ICE-CAMERA: a flatbed scanner to study inland Antarctic polar precipitation.

Massimo Del Guasta

Istituto Nazionale Ottica CNR, Sesto Fiorentino, 50019, Firenze, Italy

Correspondence to: Massimo Del Guasta (massimo.delguasta@ino.cnr.it)

Abstract.

Studying precipitation at very high latitudes is difficult because of the harsh environmental conditions that limit the external activity of humans and instruments, especially in the polar winter. The direct monitoring of ice crystal habits and size distribution in antarctic precipitation is important for the validation of the algorithms used for retrieving precipitation from ground-based and satellite-borne radar instruments, and for the improvement of the climatological modeling of polar areas. The paper describes an automated device (ICE-CAMERA) specifically developed for the imaging, measurement and classification of ice precipitation on the Antarctic high plateau. The instrument gives detailed information on precipitation on an hourly basis. The article provides a description of the device and its image processing software. Starting in 2014, the instrument operates *almost* unattended all year round at Concordia station, Antarctica (75°S, 123°E, 3220 m altitude).

1. Introduction.

In Antarctica, the characteristics of ice precipitation depend greatly on the region. In coastal areas, precipitation is influenced by synoptic scale features, such as cyclones and fronts (Bromwich, 1988). In the interior (> 2500 m), a significant part of the precipitation falls in the form of small ice crystals ("diamond dust", DD) under clear-sky conditions (Fujita and Abe, 2006). Snow particles over Antarctica are generally smaller compared to other regions of the world. The largest particles are found close to the coast, where more water vapour is available and diameters up to 10 mm are recorded (Konishi et al., 1992) with particle shapes similar to mid-latitude ones (Satow, 1983). Most of the bigger particles are aggregates (some can be found in the dataset of Grazioli et al.,2022). More inland stations record snowflakes of much smaller sizes, ranging from particles smaller than 100 μm at South Pole (Walden et al., 2003, Lawson et al., 2006) till hundreds of μm at other inland stations (Lachlan-Cope et al., 2001).

In situ measurements of precipitation are rare in Antarctica and affected by large uncertainties. This is particularly true in the high plateau, where less than 20 cm of snow accumulates every year (Palerme et al.,2014). As a result, the global precipitation products that rely on these observations (i.e. the Global Precipitation Climatology Centre (GPCC), (Schneider et al., 2017)) have no coverage over this region. Other observational products, such as the Global Precipitation Climatology Project (GPCP) (Huffman et al.,2001) , that uses GPCC for bias correction over land, has relied on satellite-only precipitation estimates. Satellite products also face large uncertainties over cold regions such as Antarctica due to insufficient sensitivity of sensors to detect and estimate precipitation signals, complex surface emissivities, and poor understanding of precipitation microphysics. Ground based K-band radars (~1-cm wavelength) are robust instruments successfully employed for studying precipitation in coastal Antarctic sites (Souverijns et al., 2017) but are quite blind to the sub-millimetre ice particles encountered on the plateau, due to the relationship D^6 between the radar scattering cross-section and the particle diameter (D).

 The satellite-borne radar CloudSat (Liu, 2008) did provide a quantum leap in observing ice in the Antarctic atmosphere (up to 82 °S), but being a single-frequency radar (like K-band radars), the retrieval of precipitation quantities relies on many assumptions about the properties of particles, resulting into ±50% uncertainties for IWC (Heymsfield et al.,2008). The microphysical assumptions (shapes and size distribution of particles) are the biggest causes for IWC, IWP, and snowfall rate retrieval uncertainty (Hiley et al.,2011, Wood et al.,2015). Moreover, CloudSat bins close to the ground cannot be used for precipitation retrieval, resulting into a severe underestimation of the diamond-dust and blowing-snow contribution to Antarctic snow balance (Palm et al., 2018). Despite these uncertainties, in absence of ground validation CloudSat data are now used as

43 independent data set for the validation of precipitation models in Antarctica (Palerme et al.,2014, Palerme et al.,2017).

44 The direct observation and the continuous monitoring of habit and size distribution of precipitation is therefore required in

45 order to validate both precipitation models, CloudSat and radar algorithms on the Antarctic plateau.

46 Disdrometers are robust *in-situ* devices, increasingly used in Antarctic coastal areas (Souverijns et al., 2017, Bracci et al.,2022).

47 They provide the size distribution and falling speed of hydrometers, but they give no direct information about the shape. The

48 evolution of disdrometers into 2D-disdrometers gave access to some shape indications about hydrometeors (Grazioli et

49 al.,2014). A further evolution of disdrometers into Imaging-disdrometers, such as the Snowflake Video Imager (SVI) (Newman

50 et al., 2009), provided realistic images of the crystals. Grazioli et al., (2017), as part of a multidisciplinary field campaigns,

51 deployed a multi-angle snowflake camera (MASC) to take photographs of individual snow particles. This instrument,

52 representing a further advance in the field of imaging disdrometers, collects high-resolution stereoscopic photographs of

53 snowflakes in free fall while they cross the sampling area (Garrett et al., 2012), thus providing information about snowfall

54 microphysics (Praz et al., 2017). The optical structure of the imaging-disdrometer and the MASC makes these instruments

55 reliable in the presence of millimetre-sized hydrometeor precipitation. In Antarctica, their practical application is mostly

56 limited to coastal zones where particles are coarse (e.g. MASC resolution is 33 μm).

57 The direct observation of inner Antarctic particles requires imaging techniques with resolution of a few microns. Photographic

58 studies of precipitation in the interior of the Antarctic are quite rare, carried out primarily at the South Pole Station (SPS)

59 through formvar replicas. In early works with formvar, Hogan (1975) identified at SPS millimetre-sized columnar crystals and

60 column- and bullet-rosettes in cloud precipitation, and smaller ($\cong100$ μm diameter) platelike particles in clear-sky

61 precipitation. Satow (1983), working with formvar replicas on Mizuho plateau found prevalently single bullets and

62 combination of bullets. Long solid column crystals were also found (with an air temperature range from -42°C to -56°C) with

63 a mean length of 290 μm and a maximum length of 1.2 mm, with a mean aspect ratio of 18. Small (50-400 μm) hexagonal,

64 triangular, scalene and square plates were also observed. Kikuchi and Hogan (1979) collected formvar replicas of DD in the

65 summer at SPS, finding columnar crystals of 90 μm average lengths and plates as small as 50 μm in diameter. Ohtake and

66 Yogi (1979) classified winter ice crystal precipitation in Antarctica under six categories. These included large rosettes, bullets

67 and columns (millimetre-sized), thin hexagonal plates and columns (200 μm or less), and smaller crystals of various shapes

68 including triangular and polyhedral. Shimizu (1963) observed "long column" crystals in the winter at Byrd Station (80S,

69 120W). Size distributions of Antarctic DD in winter and spring were reported by Smiley et al. (1980) for particles larger than

70 50 um: they observed the same ice crystal forms that were reported earlier. Walden et al. (2003) studied DD, blowing snow,

71 and cloud precipitation in winter, at SPS, by collecting crystals on slides and analyzing them using microphotography. In their

72 study, columns with an average length of 60 μm and plates with an average diameter of 30 μm were found in DD. The direct

73 observation of ice precipitation on the plateau was typically carried out by means of formvar replicas and/or microphotography,

74 but these techniques take time, are difficult to implement throughout the year and are necessarily limited to short field

75 campaigns and samples of very limited size. Designing automatic instruments for the continuous, photographic study of

76 precipitation in such a harsh environment necessarily require several compromises between the high resolution of

77 microphotography and the robustness of outdoor optical instruments such as disdrometers. Lawson et al. (2006) worked at

78 SPS, in summer, using innovative Cloud Particle Imagers (CPIs), which replaced formvar replicas. This technique allowed the

79 automatic analysis of around 700,000 DD crystal images in terms of caliper size, aspect ratio and other shape parameters. An

80 automatic classification software, based on shape parameters, was used to categorize the images into nine simplified classes:

81 small plates and spheroids, columns, thick plates, plates, budding rosettes, rosettes, complex with side planes, irregulars.

82 Concordia International Station, located on the Dome-C (DC, 75°S,123°E, 3220 m above sea level) is a special location to test

83 new instruments for precipitation studies. Surface temperatures seldom exceed -25°C in summer, whereas winter temperatures

84 can reach -85°C. The 3 m average wind speed is 3 ms^{-1} for Aristidi (2005) and 4.5

85 ms^{-1} (hourly-averaged) for Argentini et al. (2014). The strongest winds (up to 15 ms^{-1}, hourly-averaged) blow from the

continental regions. These winds are due to gravity flows from the inner plateau regions south of Dome C, and are more often observed during the winter, especially in coincidence with warming events. The circulation at the surface during the summer is affected, especially in daytime, by the synoptic circulation. In summer the wind speed oscillates during the day, with values increasing (by a few ms^{-1}) in the afternoon, when a convective layer develops, leading to the increase of the wind speed (Argentini et al.,2014). Relative humidity relative to ice is typically around 55-85% (Genthon et al., 2022). In these conditions, precipitation of ice crystals can be studied by simply collecting them on horizontal surfaces. This is done at DC by hand, starting in 2008, collecting precipitation on flat surfaces ("benches") and visually inspecting it. This analysis is restricted to one observation per day, a rate that is difficult to increase, especially in winter. The analysis of these samples is also time-consuming and often subject to biases due to ice re-processing and sublimation, hoar formation, and subjective judgement of the shape and relative abundance of ice particles. Schlosser et. al (2017) relied on this manual observation and classification of ice particles in his analysis of precipitation isotope data at DC. They classified the ice grains into diamond dust, drifting snow, snow and frost (hoar). The prevalence of hoar in the observed daily precipitation record (with temperatures below -50°C) indicates the limitations of this manual technique if detailed information on DC precipitation particles is desired.

 Detailed work was carried out in DC on a few individual DD and cloud precipitation crystal replicas by means of SEM electron microscopy by Santachiara et al. (2016). They also analyzed very small particles (10-50 μm), in a size range inaccessible to ordinary   optical   methods.
The purpose of developing ICE-CAMERA was to fill a gap in precipitation monitoring at Concordia with a robust instrument capable of monitoring with continuity, all-year round, habit and size of ice particles in precipitation, while avoiding some of the problems associated with the visual inspection of precipitation. This was achieved through the combined development of robust camera equipment and machine learning techniques for sizing and classifying ice crystals.

2. The instrument.

2.1 Overview of ICE-CAMERA.

ICE-CAMERA is a flatbed scanner (Zheleznyak et al, 2015), whose operating principle is the same as that of ordinary flatbed scanners in offices. In the case of ICE-CAMERA, it specially designed for observing polar precipitation in the harsh environmental conditions of Concordia station (Fig. 1). Within this work, the term "precipitation" will include both "diamond dust" and cloud precipitation.
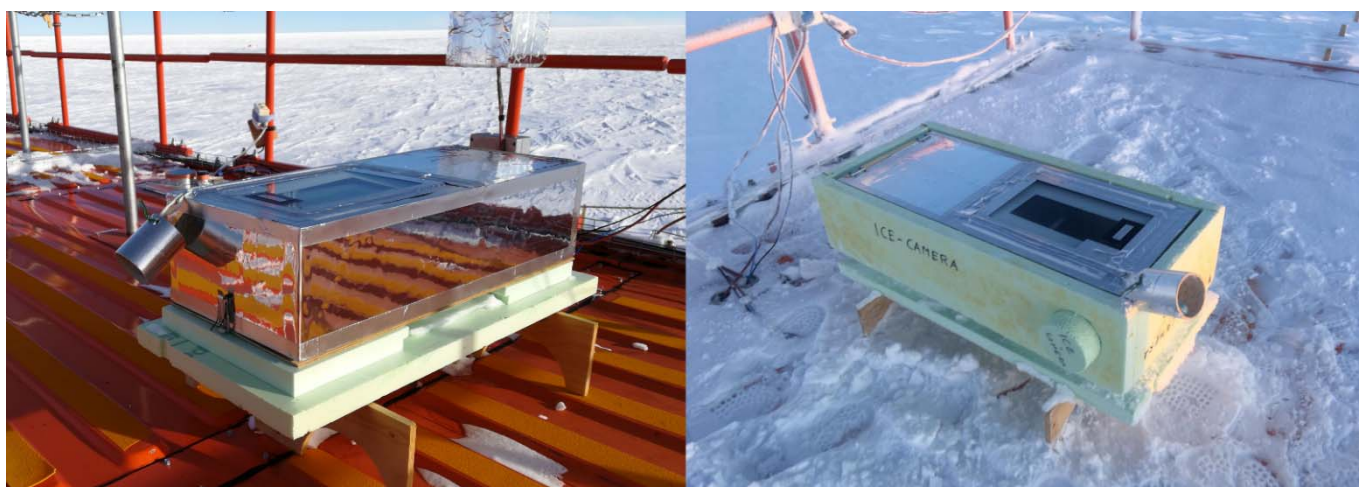
Fig. 1: ICE-CAMERA with its summer sun-shield (left) and with the winter coat (right).

119

120   The principle is simple: at the low temperatures and low wind speeds typically encountered at DC, precipitation falling on a

121   horizontal glass surface ('deposition surface', DS) accumulates with time until it sublimates, leaving enough time for scanning

122   the glass surface for counting and measuring individual ice particles. The scanning, like in ordinary flatbed scanners, is

123   performed by means of a line-scan camera (Sect.2.2). moved by a motorized scan sledge, and looking up at the DS through a

124   45° mirror (Fig. 2). The focus of the camera is adjusted by a small motorized focusing sledge moving the 45° mirror (Sect.2.3).

125   During the scan, the image is sent to the PC, located inside the shelter.

126   After a complete scan of the DS, the glass is heated and the precipitation sublimated (section 2.7). Once cooled down, the

127   clean SD begins to accumulate new particles. This cycle takes place every hour. After each image acquisition, the MATLAB

128   image processing code is called to process the DS image, and a summary-image containing only segmented particles (if

129   present) is stored for post-processing. (Sect. 4.1.3). Every particle is also automatically measured through image processing

130   (Sect. 4.1) and classified through machine learning (Sect.4.2). Individual particle data are stored in rows in a text file, along

131   with weather and housekeeping data, for post-processing and statistical analysis.

132
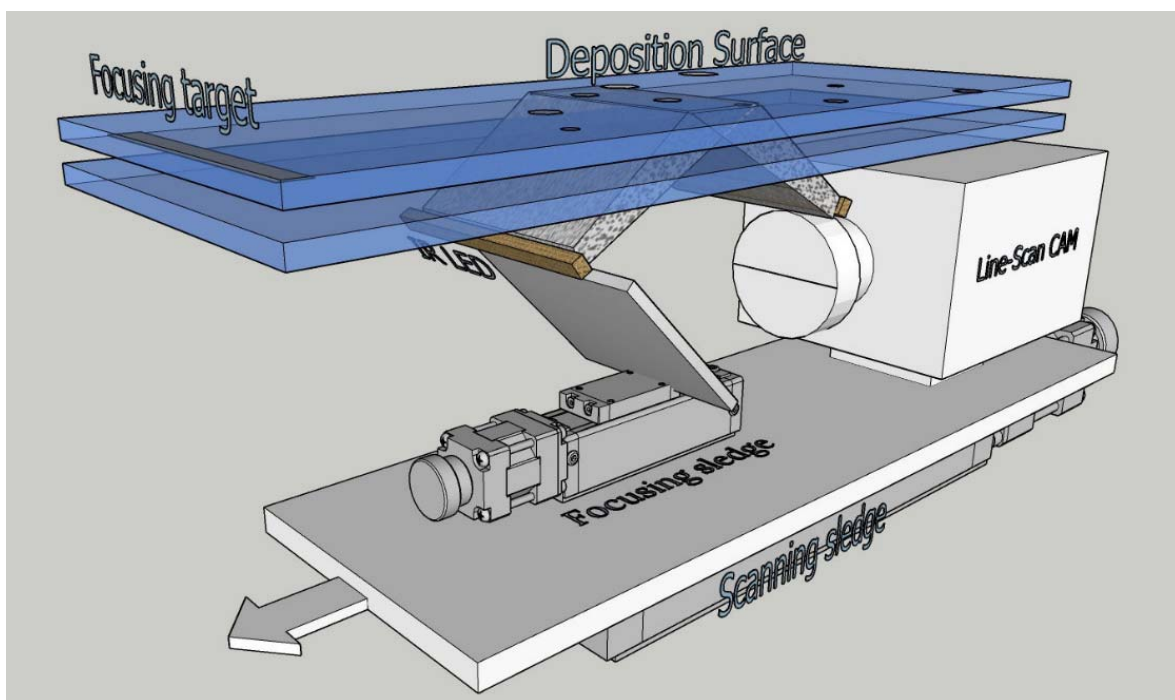
133

134   **Fig. 2: ICE-CAMERA basics: the scan sledge moves the image-acquisition line along the deposition surface. The focusing sledge**

135   **adjusts the focus.**

136

137   All basic operations of ICE-CAMERA, (with the exception of CAM acquisition) are driven by a custom microprocessor

138   (Microchip PIC) logic board (Fig. 3). The same PIC board reads the housekeeping temperature sensors (attached to the DS

139   and placed inside and outside the instrument), drives the stepper motors of the sledges as well as pumps and fans. The PIC

140   Board communicates with the main computer (located inside the shelter) through RS232. NI Labview software controls image

141   acquisition, reads maintenance data, and monitors PIC operations along the RS232 line. The line-scan camera communicates

142   with the PC via Gigabit Ethernet.

143   The instrument is placed outdoor, on the roof of the "Physique" shelter, approximately 6 m above the ground.

144   ICE-CAMERA was first installed in Concordia in 2012, but replaced in 2014 with its improved version, described here.

145   From then on, the instrument works year-round to produce precipitation data, every hour. Standard meteorological data are

146   automatically obtained from local weather station AWS MILOS 520.

147

148

149

150

151 **Fig. 3: Basic schematics of the instrument**

152
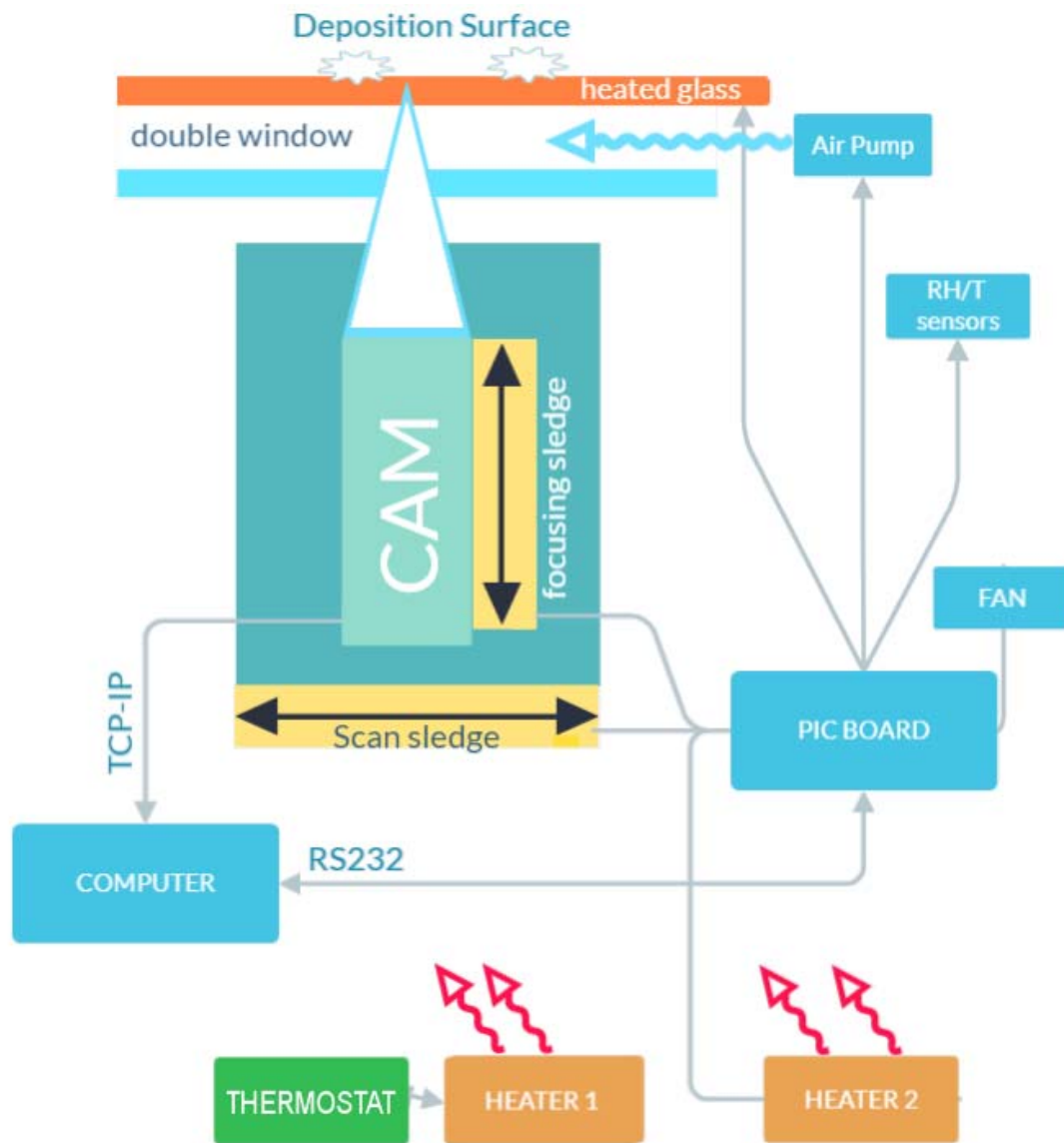
2.2 The line scan Camera.

A linear scanning GigE Vision monochrome camera (Schafter-Kirchoff SK7500VTF-XB (52.5 mm sensor, 7500 pixels, 7x7μm pixels, 8.2kHz line frequency), equipped with a 1:1 macro lens (APO-Rodagon D1X, f5.6) is used for the acquisition. The optics were designed by Schafter-Kirchoff in order to have a resolution equivalent to the 7μm pixel size. The 45 deg mirror is used to look upward. The illumination is ensured by 850 nm LEDs. A colour filter (Schott RG715, 800-1000 nm band-pass) was used on the CAM lens, in order to have a fully solar blind instrument. The line-scan camera assembly is moved, hourly, by a motorized sledge at a speed of 8 mm s^{-1} in order to scan the rectangular DS (55x200 mm), located at the center of the window. The final image is 7500*30000 pixel, 12 bits, monochrome. A fine calibration of the actual pixel size of the DS image was achieved by scanning a calibrated grid (0.1mm spacing) placed on the DS. This is necessary because the effective resolution of the image produced by the moving linear camera along the sledge direction depends on how fast the sledge moves. After the correction of this effect, the image pixel size resulted in 6.97 x 6.9 μm, which was extremely close to the simulated size of 7x7 μm.

2.3 The Focusing.

In working conditions, the focal depth is ±0.5 mm. A preliminary and accurate alignment of the motorized sledge plane to the DS ensures uniformity of focus across the DS at room temperature. A motorized focusing sledge, moving the bending mirror, allows to adjust the focus in operating conditions (Fig. 2). As ICE-CAMERA works outdoor at DC, it can experience a broad internal temperature range, from +5°C in summer to -45°C in winter, with quite large temperature gradients across the structure. Thermal expansion and changes in optical refractive indexes result in unpredictable changes in the focal plane. The correction of the focus is thus automatically performed, every 6 hours, by bringing the measuring sledge outside the DS, where a focusing spot (a sandpaper strip) is glued to the window (Fig. 4).
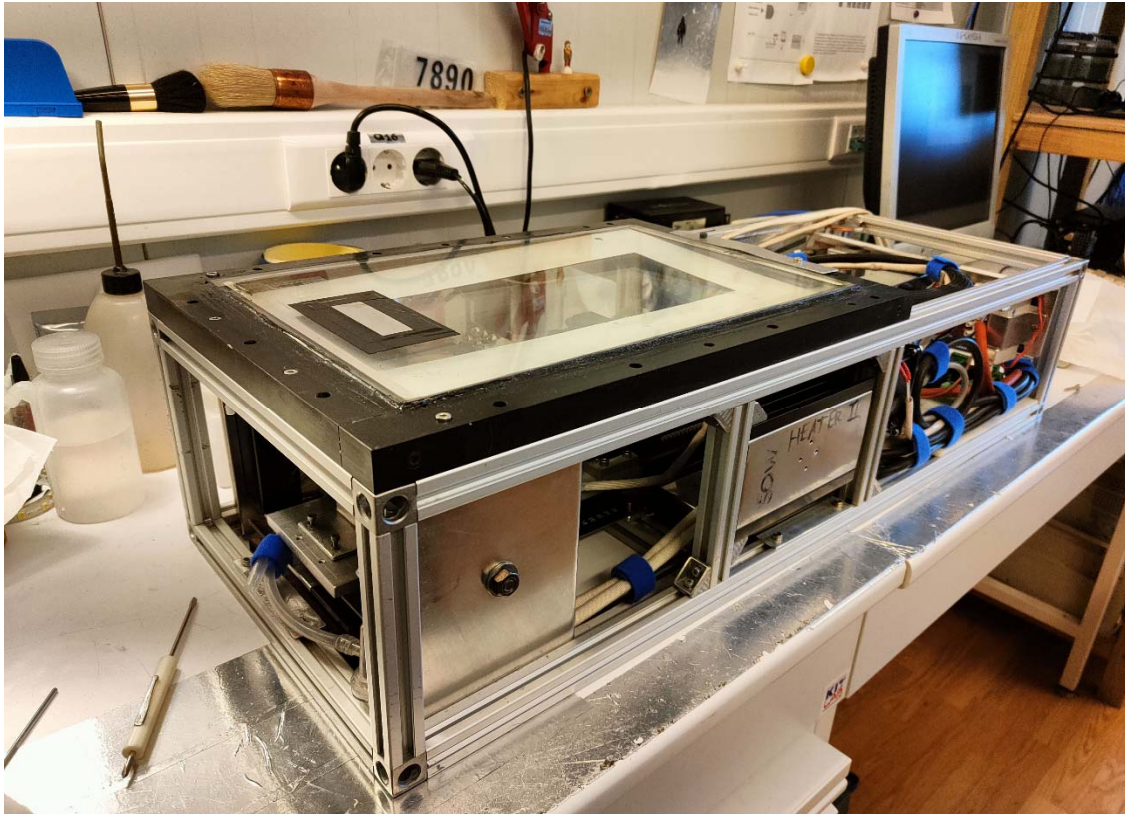
Fig. 4: ICE-CAMERA out-of-the-box. The focus target if fixed onto the DS window

The porous structure of the sandpaper has a length-scale of the order of 0.1 mm, comparable with the size of the measured ice particles. While calibrating, the focusing sledge is moved by ±2 mm around the actual position in 0.25 mm steps. Successive images of the sandpaper are taken and their contrast (defined as the standard deviation of the intensity of the pixels) is measured. After a Gaussian-fit of the contrast as a function of defocusing (Fig. 5), the position corresponding to the maximum contrast is obtained, and the mirror sledge is moved into that position. The typical focal spot adjustment between two consecutive calibrations if 0-0.25 mm. The calibration takes approximately 5 minutes. For this reason, it is not done after each measurement, so as to save PC resources for data processing.
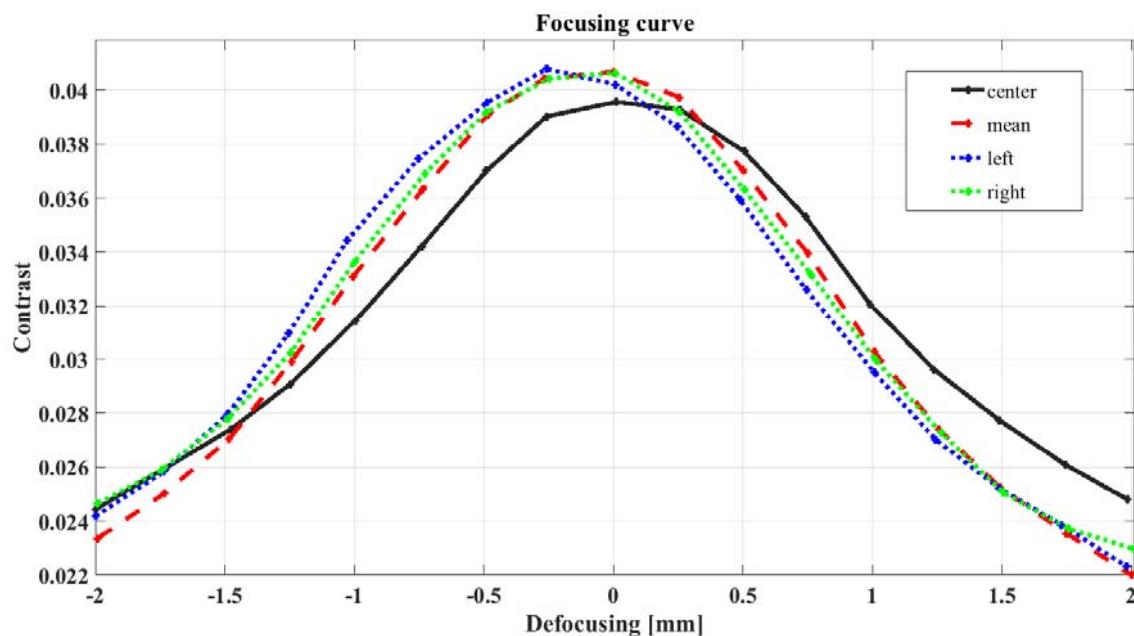
Fig. 5: Typical focus calibration: Contrast is calculated in three sectors of the image: center, left and right. The contrast throughout the image is also displayed (red). The slight difference in focus (0.2mm) between the center of the image and the side wings is a normal lens effect.

2.4 Illumination.

Lighting is supplied by two 850 nm LED (TSHG6200) strips. Both arrays illuminate the scan line symmetrically and approximately 45° from the optic axis in order to minimize multiple reflections in the double window and within the camera lens. Infrared illumination was chosen in order to work in solar-blind conditions. This is particularly important, as the linear scanning camera always looks upward, to the sky. The uniformity of lighting along the linear CCD image was tested by taking an image of the same sandpaper used in the focus. The intensity profile along the CCD image was measured, and the intensity of the LEDs eventually changed to have a final intensity uniformity across the entire frame of less than 15%.

2.5 The Deposition Surface (DS).

The DS is a 10 mm thick, electrically-heated glass (E-GLAS, Saint-Gobain). It is a sandwich with an electrically conductive layer pressed between two usual glass sheets. This glass is transparent at 850 nm, and is electrically heated with 45 V ac, 1000 Wm^{-2} when sublimating the ice particles. A second, 2 mm thick, optically graded glass sheet (an ordinary flatbed scanner optical glass), placed 13 mm under the DS, makes up with the DS a double window. This arrangement is necessary in order to keep the DS thermally insulated from the heated, interior of the instrument. A thermocouple is attached to the DS, while other thermocouples monitor window inter-space temperatures. A DS temperature of (at least) 3 °C above air temperature is enough to prevent the formation of frost on it in any season, as suggested by Tremblin et al., (2011) (Fig. 6).

Fig. 6:   ICECAMERA at -70°C, Concordia station winter: the DS if free of frost

During the sublimation period (Sect.2.7), ambient air is pumped for five minutes by means of a 3.5 l m^{-1} miniature pump through the double window space, in order to keep the internal surfaces of the double window always free of frost. Using inert gases such as argon in the double window space for the same purpose proved unsuccessful in Concordia at the extremely low winter temperatures. In order to avoid the eventual accumulation of wind-drifted snow, the DS has no walls or obstacles all around. Furthermore, the instrument is located on the roof of a shelter, almost 6 meters above the ground, an altitude where blowing snow is not normally important at Concordia. Libois et al. (2014) identify drifting snow events at Dome C when the 10-m wind speed exceeds 7 m s^{-1}. Assuming a logarithmic wind speed profile between the surface and 10-m and an aerodynamic roughness length value of 1 mm (Vignon et al., 2016), this corresponds to a wind speed threshold value of 5 m s^{-1} at 6 m above the ground. Winds below this threshold (near the annual average wind speed in DC) are not expected to carry blowing snow to the DS. In addition, blowing snow impacts the flat horizontal and smooth DS at very small angles, with a very limited chance of sticking to it. As a consequence, ice particles collected on the DS can be considered representative of precipitation. In case of strong winds, not only the attachment of blowing snow to the DS is very low, but also the collection of eventual precipitation is reduced. Since DS is warmer than air, there is no secondary growth in deposited ice. Instead, the partial sublimation of ice particles before scanning could not be excluded, especially in summer. This topic needs additional field work and will be modelled in Sect. 3.2.

2.6 The thermal control.

The temperatures measured by the ICE-CAMERA sensors are continuously transferred to the computer. The NI-Labview software controls the internal temperature of ICE-CAMERA above -40°C (by driving the 200W, ventilated resistance "Heater 2" of Fig. 3), and the DS temperature always under -5° (by eventually disabling the "heated glass" of Fig.3). These conditions are maintained throughout the year during every phase of the measuring cycle. An independent 200W wired thermostat ("Heater 1" in Fig. 3) provides emergency temperature control in case of computer or PIC board failure. After a black-out, when the power is restored, a timer is used to heat the inside of the instrument before turning on the electronics. This is important at Concordia to prevent damage to standard electronics with typical operating temperatures of -40°C. In winter, a 40 mm thick Styrofoam coat is added around the instrument for increasing thermal insulation, whereas in summer

237 a Mylar sunscreen prevents overheating of the instrument and allows keeping the DS below -5°C in the warmest days (Fig.

238 1). Additionally, in warm weather, outdoor air is carried inside the box with a tangential fan, for better cooling of the

239 instrument.

240

241 **2.7 Sublimation-deposition cycle.**

242 After an entire scan of the DS, electricity is applied to the window to sublimate the particles. The heating rate of the DS

243 depends primarily on the electrical power applied to the window and the thermal constants of the heated window, and

244 secondarily on the wind speed. An indoor test (Fig. 7), showed a heating of rate of 2.5°C min^{-1}, and a cooling rate of 1 °C

245 min^{-1}.

246
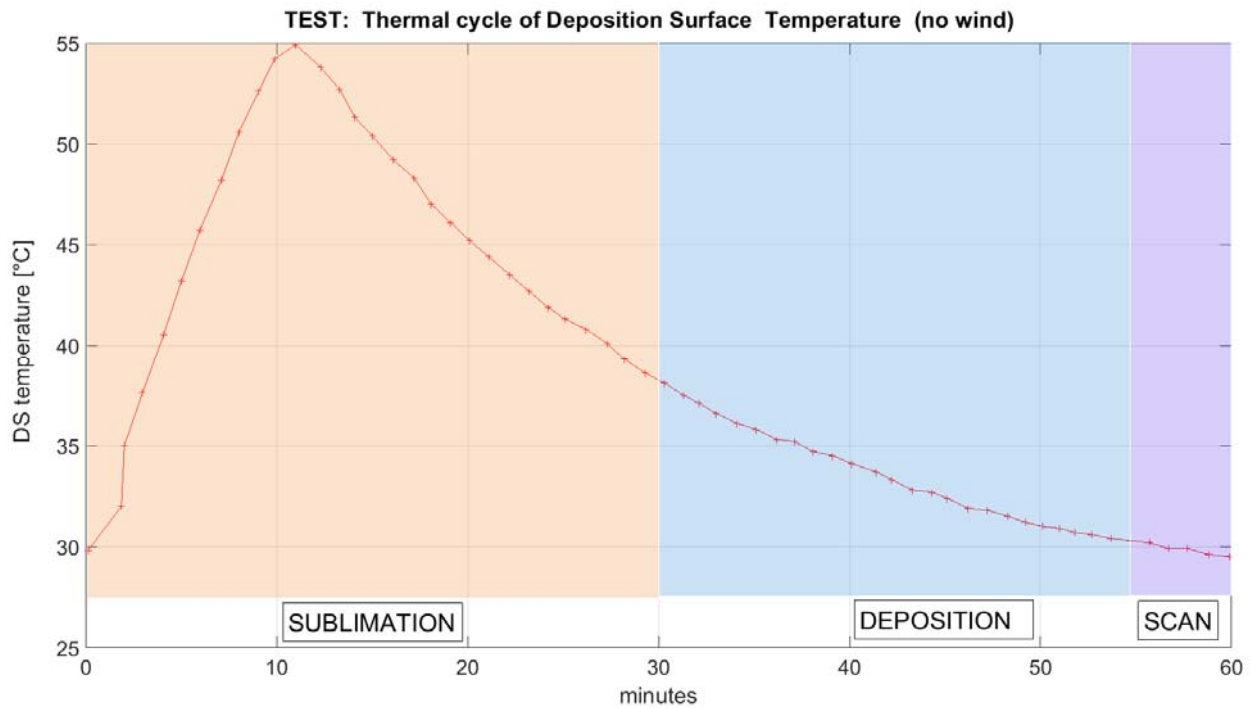
247 **Fig. 7 : Indoor test of DS heating-cooling rates within a 60 min cycle. Sublimation, Deposition and scan periods are shown**

248

249 The cooling rate is at most only about 50% of the heating rate. The cooling is passive by heat transfer to the surrounding air.

250 The sandwich-like structure of the heating-glass, with the heating layer at the middle, is depicted in Fig. 8. The conductive

251 heat transfer coefficient of the glass ($k1=0.8$ W m^{-1} K^{-1}) is much greater than that of still air ($k2=0.024$ W m^{-1} K^{-1} ; when

252 radiative cooling, convection and wind are taken into consideration, the k2 constant increases). During glass heating, heat is

253 transferred rapidly to the DS from the electrically-heated inner layer, while during cooling the heat transfers from the DS to

254 the air occurs slowly, with a thermal constant k2. This explains the asymmetrical curve of Fig.7.

255
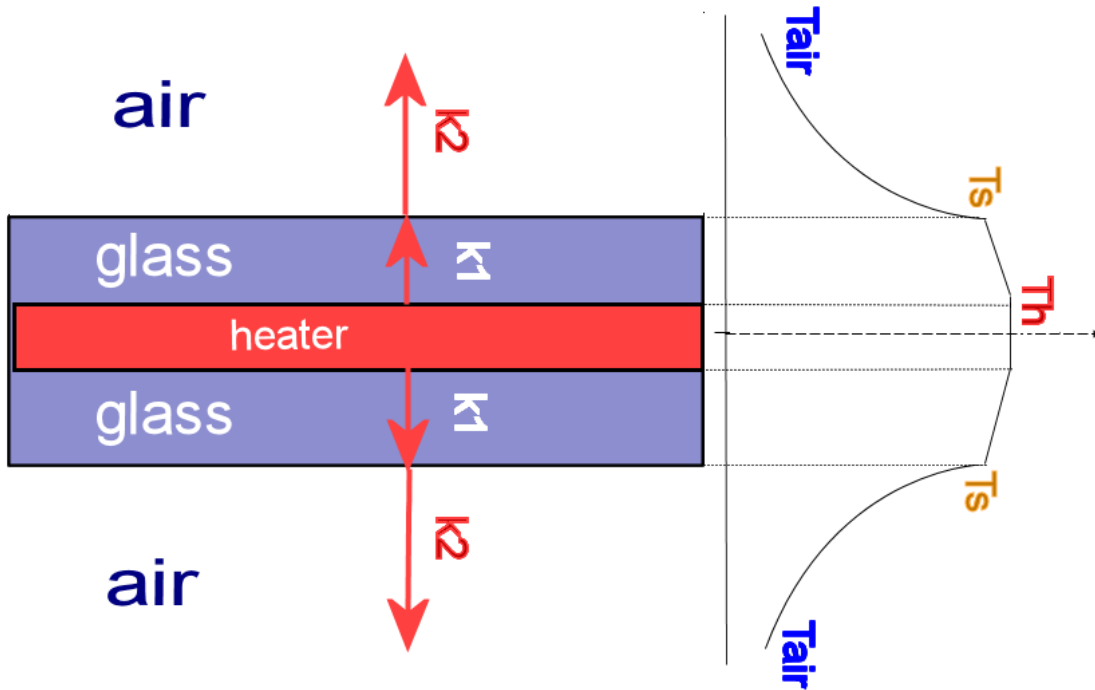
Fig. 8: left: The thermal structure of the electrically-heated glass forming the DS. k1 and k2 are the thermal conductivities of glass and still air, respectively. Right: The temperature profile during heating is sketched. Th, Ts and Tair are the temperatures of the heated layer, DS and air, respectively.

264 Outdoor tests carried out in summer at DC (-30°C air temperature) showed a heating rate of 3 °C min^{-1} in still air, 2.5 °C min^{-1} with 2.5 m s^{-1} wind speed, and 1.8 °C min^{-1} with 5 m s^{-1} wind speed. In all cases, the cooling rate was approximately 1.5 °C min^{-1}.

267 An outdoor sublimation test (-30°C air temperature, wind speed <3m s^{-1}) performed with snow manually spread on the DS

268 showed that, after applying heating for 10 minutes (up to a DS temperature of -8°C) the sublimation of the majority of particles

269 (diameter<1000 μm) was complete within 20 minutes after turning off the heating, with just a few big grains (initial

270 diameter>1000 μm) still present after 30 minutes.

271 After these tests, the glass heating period was set at 10 minutes (the heating is stopped anyway if the DS temperature exceeds

272 -5°C to avoid melting of the ice in summer). At the peak of the sublimation period, DS resulted warmer than air of about dT

273 = 20°C. Once the heater is turned off, and after a cooling time of 20 minutes, the DS temperature comes back warmer than

274 the air by about dT = 5°C. The "sublimation period" is considered complete, and ice particles accumulate again on the DS,

275 with no relevant sublimation ("deposition period" in Fig. 7). At the end of the deposition period, a scan of the DS is carried

276 out, for a duration of one minute. If no ice particles were detected on the previous scan, the DS heater is not applied, sublimation

277 is not needed. The effective deposition period depends on the temperature, wind and exposure to the sun in summer. This

278 uncertainty, combined with occasional wind removal and particulate sublimation (Sect. 3.2) during the deposition period,

279 prevents the use of ICE-CAMERA for rigorous quantitative precipitation studies.

280 DS surface temperature is actually measured by using a small thermocouple. This measurement implies great uncertainties due

281 to the radiant warming of the sensor in summer and the difficult thermal coupling with the glass surface. A non-contact

282 measurement of DS temperature by means of IR sensors would also be uneffective in winter conditions.

283

284 **3. Ice particles and the deposition surface.**

285 **3.1 Adhesion of ice particles on the DS.**

286 The adhesion of ice crystals to the smooth DS is caused by two principal reasons: Van der Waals and electrostatic forces.

287 Eidevåg et al (2020) studied the adhesion of dry snow particles after 90° impact to different wall materials. They considered

288 models for normal direction, tangential sliding, and tangential rolling that account for the adhesive Van der Waals interaction

289 of spherical ice particles (25-275 μm diameter) and their aggregates. The Johnson-Kendall-Roberts (JKR) model for adhesion

290 was used. Their findings showed that the maximum normal velocity at which spherical ice particles adhere to a glass surface

291 decreases with particle diameter. Spherical particles of 100 μm would adhere for speeds less than 0.02 m s^{-1}. In the case of

292 agglomerates with a diameter of 315 μm, composed of 1000 spherical ice particles 25 μm diameter each, the sticking velocity

293 for the adhesion of 90% agglomerates normally hitting the surface increased to 0.5 m s^{-1}, just one third of the Stokes

294 sedimentation speed (1.7 m s^{-1}) calculated for the same aggregate at DC conditions (Tair=-50°C , air density=1.03 kg m^{-3},

295 dynamic viscosity= 1.44E-5 Pa s). These results show that the 300 μm diameter ice particles could stick to the ICE-CAMERA

296 window for the weak Van der Waals' forces alone. Ryzhkin and Petrenko (1997) showed that static charges, naturally

297 transported by ice crystals, increase adhesion. The electrostatic interaction between the ice and the surface is significantly

298 stronger than the van der Waals forces at distances greater than the inter-molecular forces. This effect explains why the «big»

299 ice crystals (D>300 μm) also adhere to the DS. Once attached to the DS, the weak winds generally observed at DC cannot

300 detach the particles from the DS. Particulates are protected by the boundary layer (BL) that forms on the DS. The 99% thickness

301 of the laminar BL (Blasius solution) at the centre of the DS (0.15 m distance from the window edge) is expected to be 7 mm

302 at -50°C with a wind speed of 1 m s^{-1}, decreasing to 2 mm at 10 m s^{-1}. As a result, the particles deposited on the DS are

303 protected against the wind.

304

305 **3.2 Sublimation of ice particles.**

306 The DS of ICE-CAMERA is always warmer than the surrounding air. This is necessary to eliminate hoar, enabling the device

307 to be used in all DC conditions. The adverse effect is an accelerated natural sublimation of deposited particles. A wide range

308 of experimental and theoretical research efforts has characterized the effects of temperature and super-saturation on ice crystal

309 growth rates and morphology under conditions relevant to atmospheric processes (for example Lamb and Hobbs, 1971;

310 Libbrecht, 2005; Libbrecht, 2017). The wide variety of ice crystals found in nature has sparked an interest. Sublimation was

311 sometimes regarded either as the opposite process, or a less intriguing process, and was less visited in lab studies.

312 Nelson,(1988) sublimated numerous, 100 μm diameter plate crystals (0.1°C>T>-18°C, 0.05% to 5% sub-saturation) showing

313 that the crystals first lost sharp edges, and finally evolved into spheroidal particles, and the aspect ratio remained almost

314 constant. The sublimation rates were accurately predicted by the diffusion equation with the surface vapour density at the

315 equilibrium value for a uniform surface temperature. The sublimating crystal reaches a self-preserving shape that is one of the

316 shape preserving solutions of the diffusion equation. Ham (1959) showed that ellipsoids and thus spheroids preserve shape

317 during growth and sublimation if the grain surface has a uniform temperature. Jambon-Puillet et al.(2018) also showed

318 experimentally and theoretically that sublimation first smooths out regions of sharp curvature, leading to an ellipsoid. The

319 second stage is the sublimation of the self preserved ellipsoid shape. The entire process may be modelled as a vapour diffusion

320 problem, mathematically equivalent to the resolution of the electrical potential around a charged conductor. Using this analogy,

321 they provided a mathematical method for simulating the sublimation of the ice particle. The sublimation of the ellipsoid turned

322 out mathematically simple, and their method was adopted in this work to numerically simulate the second stage of sublimation

323 of ICE-CAMERA particles.

324 Monodispersed oblate spheroids with an aspect ratio (AR) of 5, in thermal equilibrium with the DS, were assumed in the

325 simulations as a surrogate for ice plates. The two major spheroid axes coincide with the «diameter» of the oblate spheroid, D.

326 In the model, D, DS temperature, air temperature and relative humidity with respect to ice (RHair) can be changed. The

327 sublimation time required for full sublimation of a spheroidal ice particle was computed. As sublimation accelerates when the

328 particle is going to vanish, the time necessary for the complete sublimation is only slightly larger than the time necessary to

329 reduce the particle to the minimum particle size (D=60 μm) accepted by ICE-CAMERA image processing. The simulations

330 assume that the preliminary sublimation of the high-curvature parts of the particle (sharp edges, corners, surface irregularities)

331 was already completed, so that the calculated time of sublimation must be considered as a lower limit for real-world crystals,

332 and probably almost one half of the overall duration of sublimation (Jambon-Puillet et al.,2018). Simulations also assume the

333 thermal equilibrium between the particle and DS, a condition which is not necessarily satisfied on the thermally insulating

334 glass surface of the DS. Figure 9a shows the total sublimation time with the DS heated dT=+20°C above air temperature

335 (sublimation period). The humidity resulted irrelevant in this case, and only results for 70% RHair are shown. Results show

336 that at -30°C air temperature (summer conditions in DC) complete sublimation can occur within a few minutes after attaining

337 the DS sublimation temperature, for all particle sizes up to 1 mm. At lower air temperatures, the sublimation time increases:

338 at -70 °C (winter temperature in DC), particles smaller than 100 μm in diameter still disappear within 10 minutes, while larger

339 particles can survive along the sublimation period. Simulations showed that, at -70 °C, dT should be increased to dT=60°C in

340 order to ensure the complete sublimation of ice particles up to 1 mm diameter during the sublimation period. This is actually

341 not possible with the electric heated window glass adopted, but could probably be achieved by microwave heating.

342
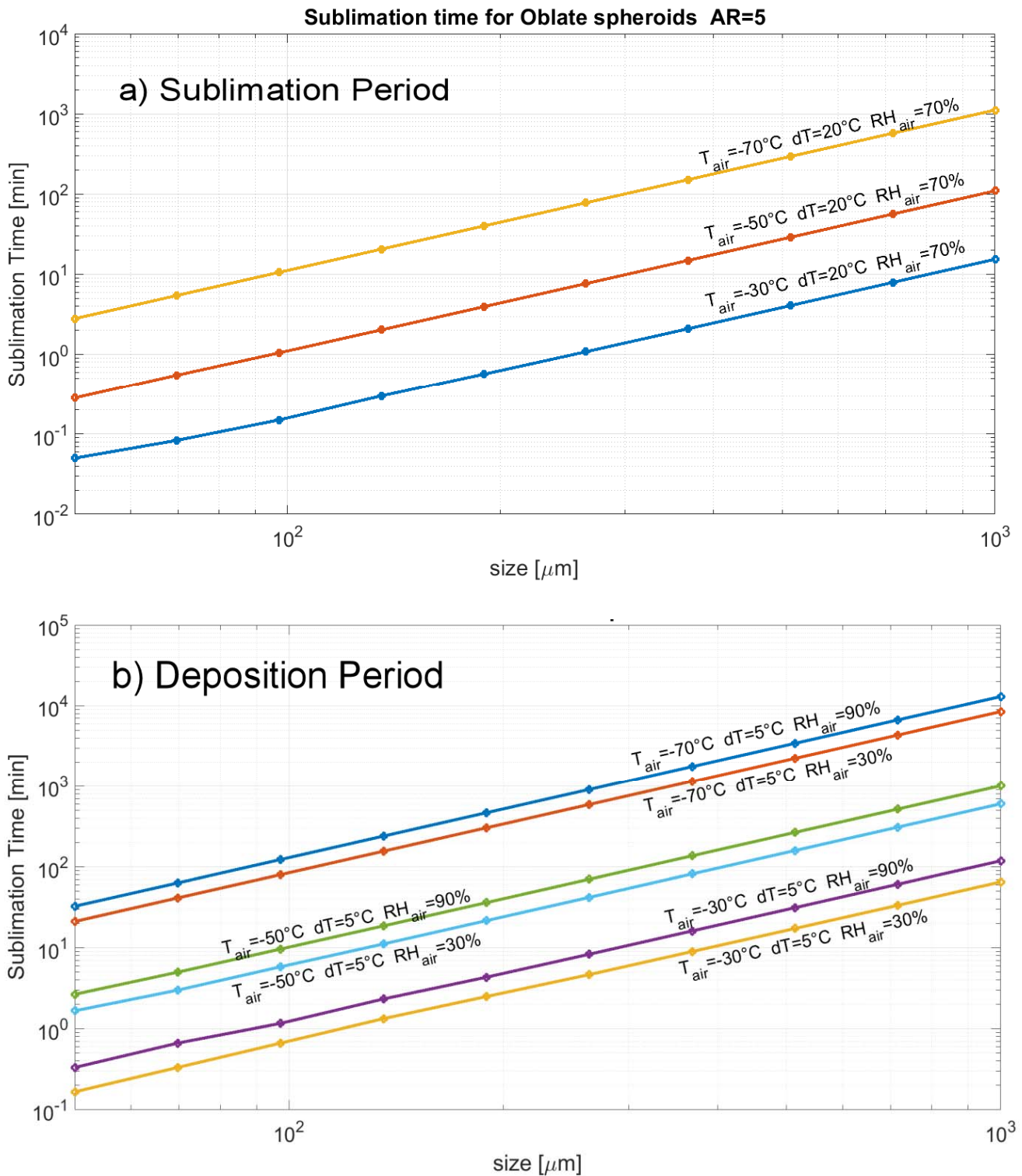
Fig. 9: Sublimation time of monodisperse oblate spheroids at varying air temperatures, with a) dT = 20°C (sublimation period) and b) dT=5°C (deposition period).

After the sublimation period, most of the particles previously collected on the DS are sublimated, and a new deposition period begins. Even during this period, sublimation still acts on ice particles, albeit slowly. Figure 9b shows the sublimation time expected for monodisperse spheroids during the deposition period. The DS was considered 5 °C hotter than air. As shown, during the deposition period the relative humidity of air also plays a role, even if secondary. In summer (Tair=-30°C), sublimation can take less than a minute for particles smaller than 100 μm and ten minutes for 300 μm particles. During winter (Tair = -70°C), all particles are expected to survive through the deposition period. As a rule-of-the-thumb, simulation showed

353 that working with dT=+5°C resulted in an increase of the rate of sublimation by a factor 2-3 compared with a DS in thermal

354 equilibrium with ambient air (dT=0) for the whole range of air temperatures and RHair shown in Fig. 9b.

355 Results of Fig.9b show that the effective lower limit of ICE-CAMERA particle detection is not limited solely to the resolution

356 of the optical system and/or image processing software. In summer, particles smaller than 100 μm may be decimated during

357 deposition, unless they fall just before scanning. Such small particles dominate diamond dust events. As a result, ICE-

358 CAMERA, during the summer period, is best suited to the study of cloud precipitation. Nevertheless, visual screening of ICE-

359 CAMERA images showed only a limited number of small particles revealing signs of partial sublimation, such as rounded

360 corners, smooth edges, or a spheroidal appearance. Some small plates (observed mainly in winter, when sublimation during

361 the deposition period is very slow) showed smoothed corners, but it is not clear if this was induced by sublimation or is a

362 natural feature of these ice grains. Also, even in summer, small DD particles such as plates (with no signs of edge smoothing)

363 were normally observed (Sec.5.2). It is probable that most particles (other than, probably, pristine plates) never achieve thermal

364 equilibrium with the DS glass, and that the results of Fig.10 should be considered as the worst case. Also, the sublimation of

365 the high-curvature parts of the particle prior to assuming the spheroidal form (Jambon-Puillet et al.,2018) could take much

366 more time than the sublimation time calculated here for the spheroid. A series of consecutive DS scans at fixed air temperatures

367 is needed to measure the effective sublimation rate of small particles in deposition conditions (dT=+5°C).

368 When a polydisperse particle population is deposited on the DS instead of monodisperse particles, a more complicated

369 sublimation picture arises, because small spheroidal particles, shrinking, are continuously replaced in the size distribution by

370 sublimating, initially bigger ones. An initial uniform particle size distribution (PSD) of the oblate spheroids (AR=5) was

371 assumed with diameters between D=1 and 2000 μm for the simulations. The evolution over time (1 sec resolution) of the PSD

372 was calculated (Fig. 10) in terms of particle survival (the ratio between the actual number of particles in a certain size bin and

373 the initial number in the same bin). No vapour competition between ice particles was taken into consideration in the

374 simulations. Results are similar to those of monodisperse particles (Fig. 9), with a slightly longer time of sublimation for

375 polydisperse particles compared to monodisperse particles of the same size. Results for an air temperature of -70°C confirm

376 that most particles larger than 500 μm survive, throughout the DS sublimation period (dT = 20°C), longer than 30 minutes.

377 This means that sublimating by heating the window is quite inefficient for large particles in winter. During the deposition

378 period, at -70°C losses for sublimation are scarce and limited to particles smaller than 200 μm. Consequently, double counting

379 of the same particle (D>500 μm) is possible in two consecutive ICE-CAMERA scans in the cold DC winter. At -30°C air

380 temperature (summer) the heating of the DS with dT=20°C leads to the sublimation of most particles up to 2 mm diameter

381 within 5 minutes. On the other side, during the deposition period particles smaller than 500 μm can undergo sublimation over

382 a period of just 10 minutes in summer, thus limiting the effective period of deposition before a scan. As with monodisperse

383 particles, this introduces bias in the summer because many small particles (typical of DD) can be removed before they are

384 measured.
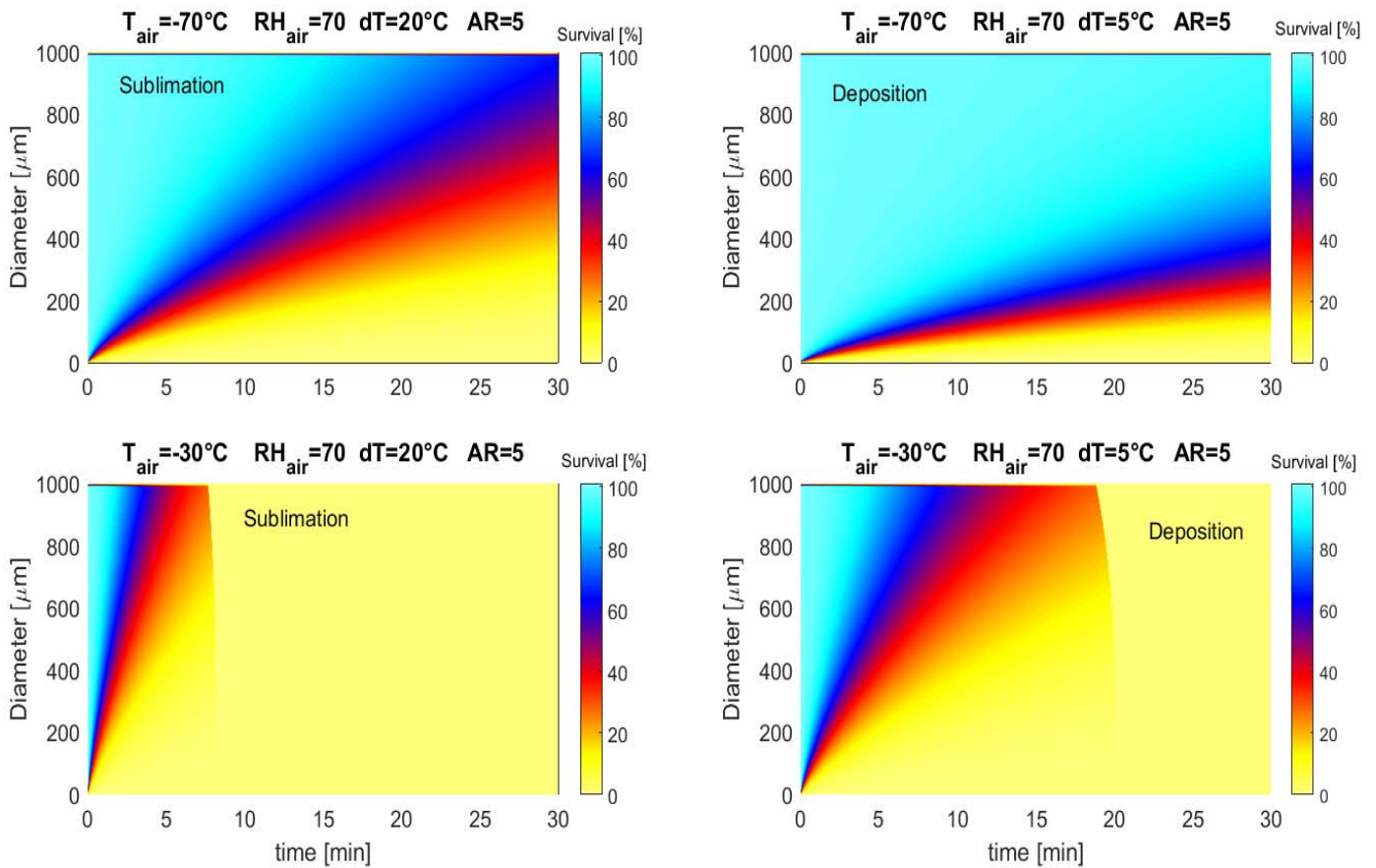
Fig.10: Evolution of a originally uniform PSD of ice spheroids (D=0-2000 μm, AR=5) under different atmospheric conditions. (RHair is a secondary factor affecting the results, shown here for RH=70%). Left: sublimation period; right: deposition period. Top: winter, bottom: summer.

Even if these results could be disappointing for interpreting ICE-CAMERA data, the same problems affect the actual method of observing precipitation in DC: collecting and observing (every 24 hours) the ice particles deposited on flat surfaces ('benches') is affected by the same problem as collecting particles on the ICE-CAMERA DS with dT=0. Fluctuations in relative humidity over 24 hours result in sublimation and regrowth of particles on the "benches" in an almost unpredictable manner. Fig. 11 shows the expected sublimation time for particles (with the same PSD of Fig. 10) placed on 'benches' (or ICE-CAMERA DS) in equilibrium with air (dT=0) for extreme, sub-saturated conditions: winter Tair=-70° (RHair=30% and 99%), and summer Tair=-30 (RHair=30% and 99%). The PSD evolution is computed with a resolution of 1 sec for a total period of 6 hours. The results show that sublimation also works in winter and with almost saturated air (99% RHair), leading to a complete loss of small particles (D<200 μm) in a few hours. In summer conditions and 30% RHair sublimation happens much more quickly, with the disappearance of all particles up to 2000 μm in 30 minutes. With RHair=99%, sublimation removes all particles in just a few hours in summer. In presence of wind and dry air, sublimation rate could even increase, as observed by Grazioli et al., 2017 in coastal areas. These simulations all refer to sub-saturated conditions: in the case of a 'bench' in thermal equilibrium with super-saturated air, hoar form on the surface, with a possible confusion with precipitation.
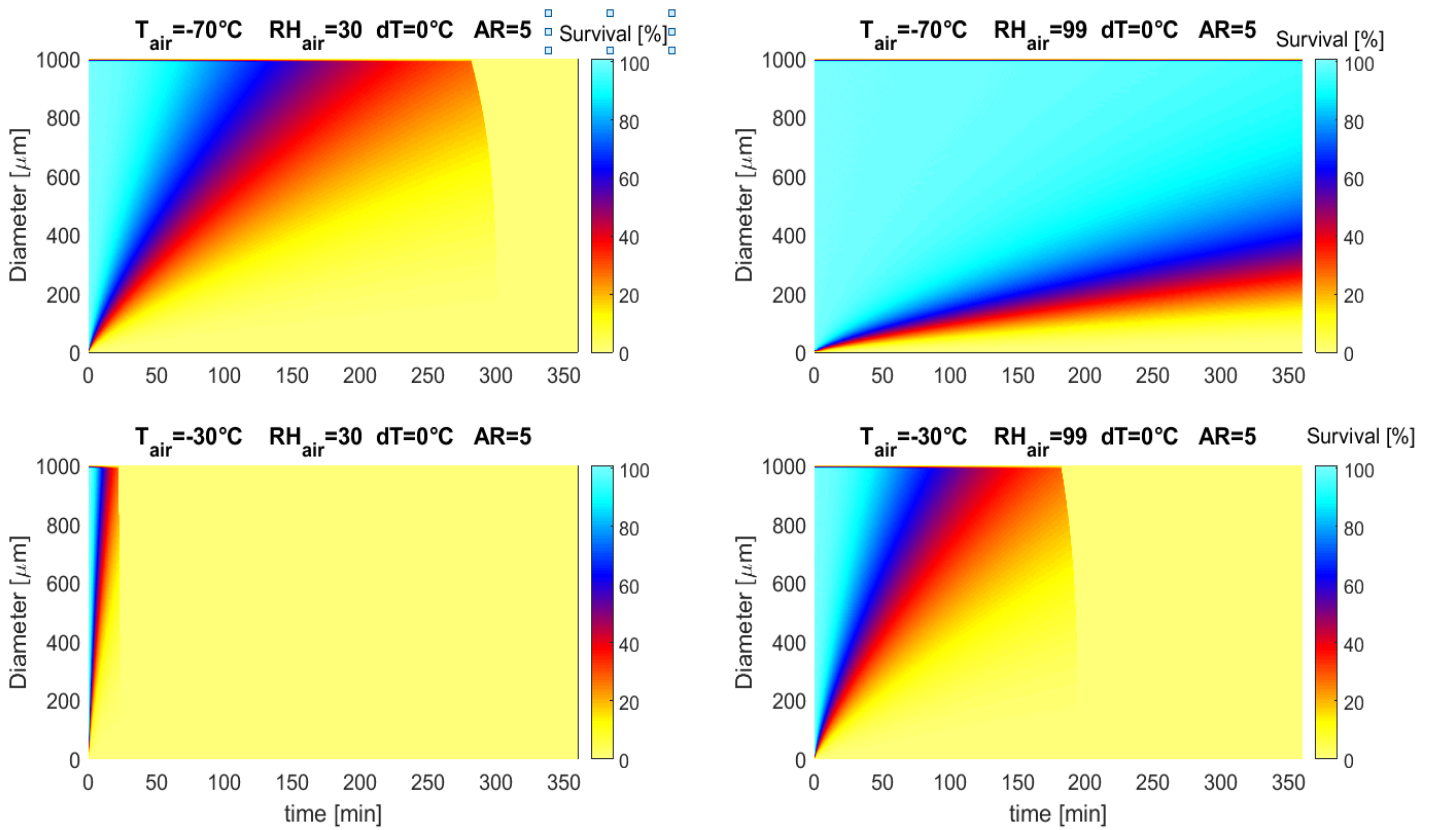
403
404 **Fig.11: Evolution of a originally uniform PSD of ice spheroids (D=0-2000 μm, AR=5) under different atmospheric**
405 **conditions. The DS (or 'bench') is in thermal equilibrium with air (dT=0). Top: winter, bottom: summer**

406

407

408 **4. Data processing.**

409

410 **4.1. Image processing.**

411 ICE-CAMERA is not just designed to take photographs of ice particles, but to provide automatic morphometry and
412 classification of polar precipitation. This was accomplished through the use of image processing and machine learning
413 techniques. The process is divided into two parts: segmentation and measuring, and classification of ice crystals.

414

415 **4.1.2 Image segmentation and measurement of ice particles.**
416 After acquisition, the raw ICE-CAMERA scans are segmented, using MATLAB software, to isolate all detected particles. The
417 process follows the workflow of Fig. 12. Refer to Pratt (2007) for image-processing nomenclature, to Walton, 1948 for Feret
418 measurement, to Russ and Brent Neal (2017) for the nomenclature of standard shape parameters such as Eccentricity, Euler
419 Number, circularity, roundness, solidity, compactness, form factor, and number of skeletal branches. The normalized central
420 moments f1...f7 were also computed as described by Hu, (1962).
421 The Aspect Ratio (AR) is defined as Feret's length/ Feret's width. The Feret-box surface-equivalent diameter (Df) is defined
422 as the diameter of the circle of the same area as the Feret bounding box, while the surface-equivalent diameter (Ds) is
423 defined as the diameter of the circle having the same area as the segmented ice grain. The main steps of Fig. 12 are visually
424 summarized in Fig.13 for a rimed, columnar particle.

425

426

427

The flow chart boxes read:

Scan → background subtraction → intensity equalization → Region growing (with normalized-intensity range: 0.2-1)

Image Segmentation and Labeling (8 pixel -connected regions) ← "majority" correction (all pixels surrounded by 4 other "one" pixels are set to "one"). ← Image closure (10 pixels)

Selection of the largest labeled region → Creating the best adapted, rotated Feret bounding box → Image rotation (horizontal box) → Image resize to CNN input size 224*224

Feret's length, width, Aspect Ratio

Feret box surface-equivalent diameter

Standard measurements :

projected surface (S)

surface-equivalent diameter (Ds).

shape parameters

(Eccentricity, Euler Number, circularity, roundness, solidity, compactness, form factor, skeletal branches)

Fig. 12: The image-processing flow chart.

Original   Reg.Growed   Feret AR=2.8 L=875 um   outlined original image   224*224 image ready for CNN
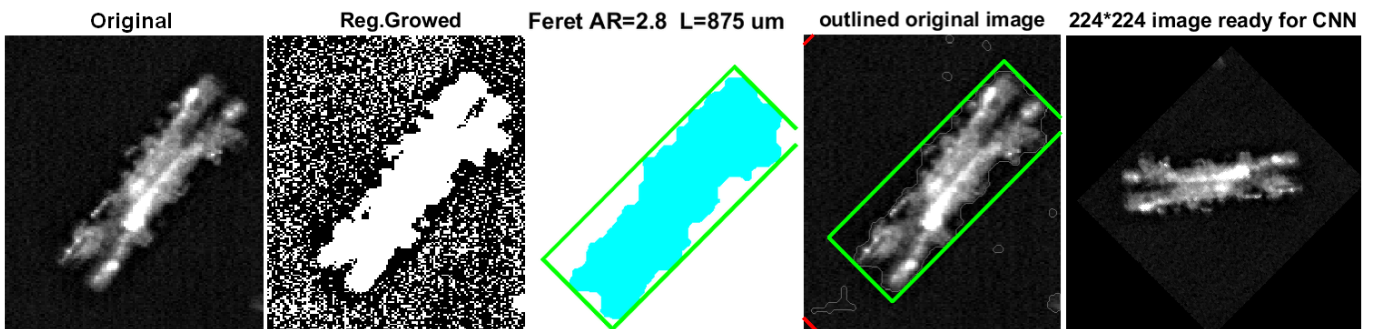
Fig. 13: The original image (in this case a rimed column) is segmented using 'region-growing'. The projected particle area (clear blue) is calculated. The bounding box is determined (green) and the Feret length and width measured. The image is finally rotated to have the mayor axis horizontal, re-scaled, and resized to the CNN input size.

445

4.1.3 Summary-image of detected particles.

The bounding boxes of all individual ice particles detected in a scan are sorted by Feret length, and reassembled in a summary-image collecting all segmented particles (Fig 14). Each particle is also associated with a numerical record containing the coordinates of its bounding rectangle on the summary-image, shape parameters, Feret size, time of acquisition and local weather data. In this way, the re-analysis of the summary-image is possible instead of re-processing the original, large image. The original image is ultimately removed.
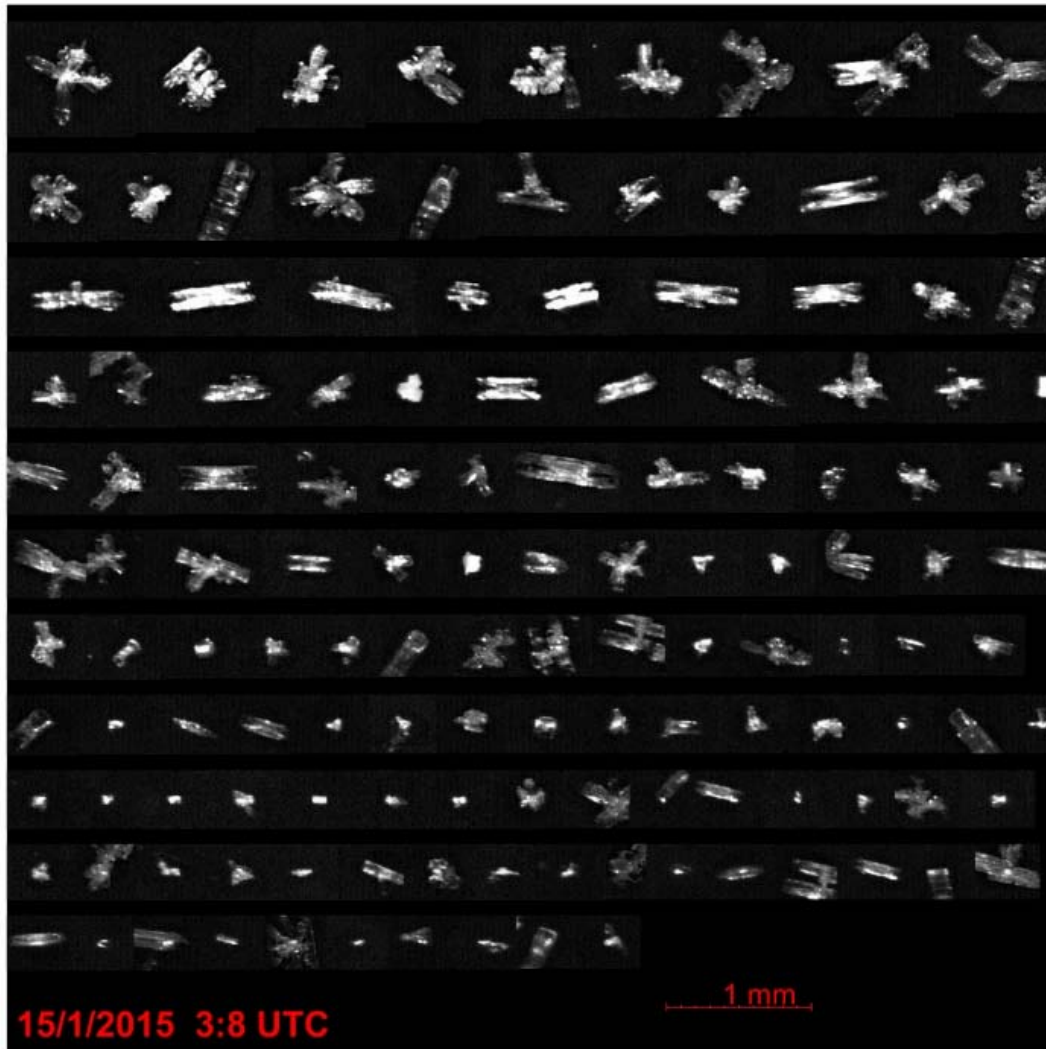
Fig. 14: Example of a summary-image for a single scan.

4.1.4 Limitations and uncertainties in detecting and sizing ice particles.

1) The total number of particles measured is limited to 2000 per scan, as a result of MATLAB memory limitations. Extra particles are not treated.

2) Particles below 3600 μm^2 in bounding-box surface, 73 pixels minimum size (equivalent to approximately D<60μm) are not preprocessed (smaller particles could be detected, but most have a seemingly circular shape due to low pixelation or poor focus).

3) The segmentation becomes difficult when overlapping particles or aggregates of particles are present. In such situations, double counting of the same particle may occur in up to 12% in a scan in the presence of an intense precipitation event. The same particles can in fact fall inside different segmented areas of the image, because of the

lack, on the original image, of defined boundaries between particles. The process of "region growing" which leads to segmented particles can actually start, independently, from several bright ("seed") regions located in different parts of the image of the overlapping particles. The 'region growing' processes can then propagate through the overlapping particles leading to several 'copies' of the same, segmented image. Overlapping particles are normally classed by the CNN algorithm as "clusters". A few occasional arrangements of three or more overlapping columns are sometimes mistaken for single plates. The Feret measurement of these particles is meaningless. At DC this situation occurs only after heavy cloud precipitation, a relatively rare event.

4) Particles close each other in the original image could be segmented into a single particle by region-growing and thus misclassified.

5) In the case of defocused images, the particle shapes are all close to a fuzzy, round or elliptical shape, which can cause a misclassification into irregular particles, spheroidal particles or plates. ICE-CAMERA images dominated by this type of particles are normally eliminated during a preliminary manual screening. Also, a few big particles in summer resulted rounded by partial sublimation. A few images containing only rounded or "spheroidal" particles of 500 μm diameter or greater were collected during the warmest part of summer, and were manually discarded before the statistical data analysis.

6) Needles and hexagonal plates (typically small, see Fig.26) may be very bright in ICE-CAMERA images due to enhanced light diffusion at preferred angles. For the same reason, hollow columns sometimes have a shiny spot in the middle. .In the case of needles, this effect can reduce the apparent aspect ratio, as the width is apparently increased by the scattered light saturating the camera. For plates, the bright specular reflection blurs sometimes the polygonal contour, especially in the case of small plates.

4.2 Automated classification of ice particles.

An initial attempt at automatic classification of ICE-CAMERA segmented images was made in 2014 using shape factors. This kind of technique has also been used by others (e.g. Lindqvist et al., 2012) for attempting the classification of ice particles. In the case of ICE-CAMERA this approach resulted extremely unreliable. A much more promising approach was offered after 2015 by the rapid development of transfer learning and convolutional neural networks (CNN) (Le Cun et al., 2015; Schmidhuber, 2014). Xiao et al. (2019) successfully applied deep transfer learning to ice particle images obtained with airborne Cloud Particle Imagers (CPI). The CNN approach has added much value to ICE-CAMERA because a reliable classification of ice particles into simplified classes became possible. The CNN used for the ICE-CAMERA particle classification is "GoogleNet" (Szegedy et al. 2015), a variant of the Inception network, a deep convolutional neuronal network developed by Google scientists. GoogleNet is a type of convolutional neural network based on the Inception architecture. It utilises Inception modules, which allow the network to choose between multiple convolutional filter sizes in each block. The GoogleNet architecture consists of 22 layers (27 layers including pooling layers), and part of these layers are a total of 9 inception modules. In this work, GoogleNet was used in MATLAB R2020b environment. The GoogleNet CNN, pretrained on the ImageNet data set (Deng et al. 2009), was used, with its final, fully connected layer changed to size 14. The input layer of the GoogleNet architecture requires images of size 224 x 224.

4.2.1 The CNN classification classes.

Low temperatures and humidity on the high Antarctic plateau reduce the diversity of ice particle shapes. This is observed on the field at DC, at South Pole station (Lawson et al., 2006), and suggested by review works such as Bailey and Hallett (2009). Following an initial survey of the ICE-CAMERA image database, a set of 14 types of particles was selected, as shown in Fig. 15. When choosing the 14 classes, I assumed that shapes easily recognizable by a human operator could also be easily recognizable by a CNN.

509

510

Needle
Bullet
Column
Hex Plate
Trig. Plate
Irr. Plate
Rosette
Irr.Rosette
Irr. Grain
Spheroidal
Frost
Comp.Column
Fiber
Cluster
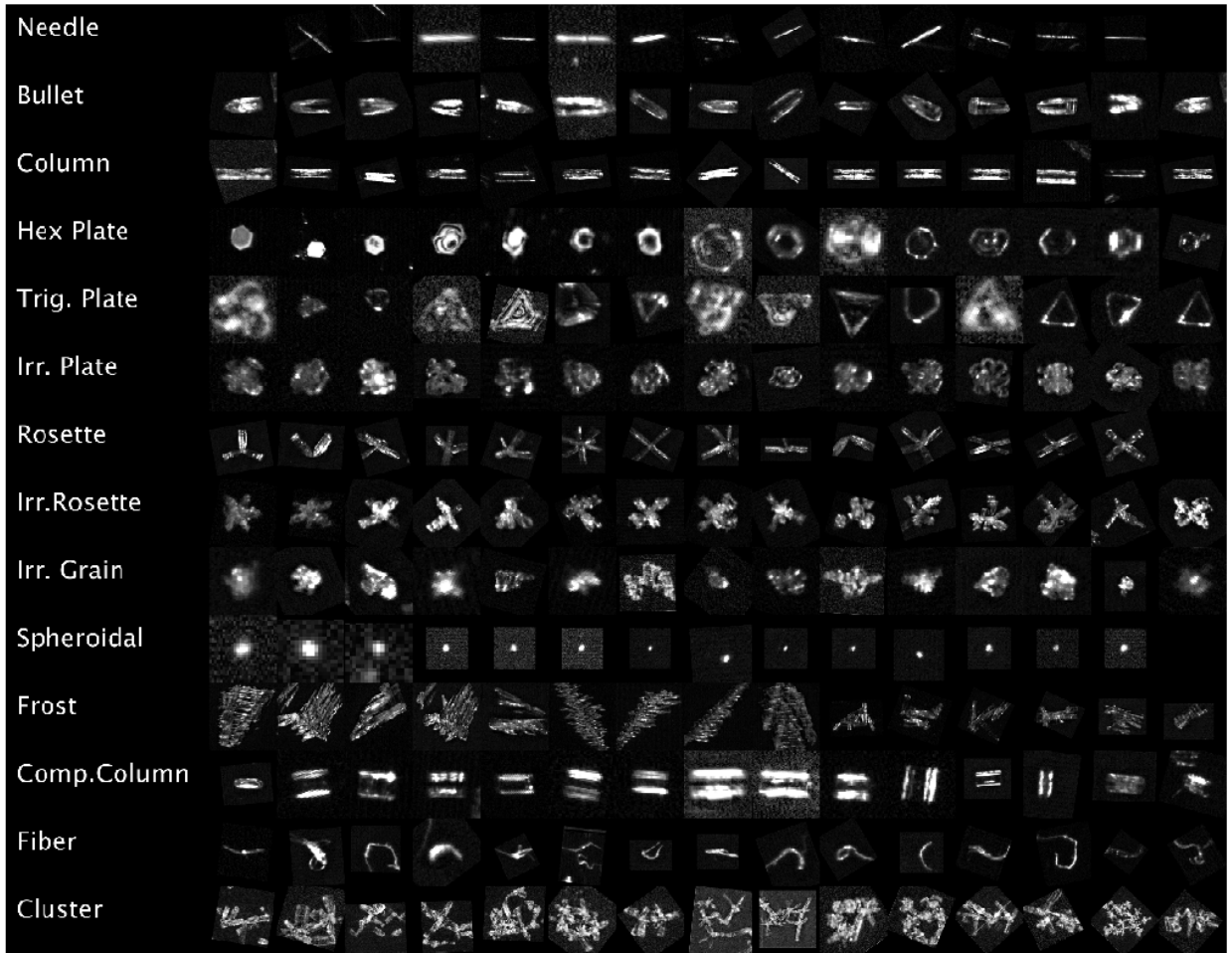
511

512   **Fig. 15: A sample of ICE-CAMERA images of the 14 classes of ice particles used to train the CNN.**

513

514   In the following scheme I tried to fit the classes chosen for ICE-CAMERA with the classification scheme of the ice particles

515   of Kikuchi et al. (2013), an updated version of the original classification of Magono and Lee (1966).

516

517   -**Needles:** covering the classes C1a,C1b,C3d   (Kikuchi et al. 2013)

518   -**Bullets:** covering the C4b-C4c classes.

519   -**Columns:** columns covering classes C2a, R2b, C3a, C3b.

520   -**Hexagonal plates:** covering classes P1a, P1b, P1c, P4f, G2a, G3a, CP3f, CP3d.

521   -**Trigonal plates:** covering the class G2b.

522   -**Irregular plates:** plate-like particles with irregularities, riming, overgrowing plates, etc. But keeping a basic hexagonal

523   shape, covering P6a, P6b, P7a, CP6d, R1b, R2b, R2c, R3a, G4b.

524   -**Rosettes:** bullet-rosettes or column-rosettes, with a minimum of two branches, covering C2c, C3e, C4d

525   -**Irregular rosettes**: rosettes with irregularities, riming, but preserving the typical stellar outline of rosettes. Covering

526   classes P7a,P7b,CP2d ,CP4c,CP5a,CP6e,CP6f,CP6g,R1d

527   -**Irregular grains:** covering CP3e, CP5a, CP6d, G4c,G4a,I3a,I2a,I1a,H1a,H1b

528 **-Spheroidal:** particles with spheroidal or spherical appearence, covering H1a, H1c. (Large particles with D>600μm)

529 detected as 'spheroidal' in DC are usually artifacts caused by defocused images and are not considered in the statistical

530 analysis.

531 **-Compact columns:** short columns covering classes G1a, C3a

532 **-Clusters of particles:** covering A1a, A3a, H2a, H1b, P8b, CP3e, CP5a, CP6h

533 **-Frost**: frost formed on the DS plate CP7,CP8,CP9

534 **-Fibers**: non-volatile fibrous material (from local human activities, Styrofoam particles, textile particles, dust, etc)

535

536 The last two classes are not considered in the statistical analysis of ICE-CAMERA data: they are just used to detect occasional

537 frost formed on the DS, and man-made, non-evaporable (thus persisting on the DS) materials. Uncommon ice particle

538 typologies present at Concordia were not considered in the present work. Trigonal plates have been included, although they

539 are rare, simply because they are seemingly easy to detect with CNN.

540

541 **4.2.2 The training data-set.**

542 For the first CNN training, a set of 5500 ICE-CAMERA segmented images of single particles, sampled randomly from the

543 2014-2017 ICE-CAMERA database, have been manually sorted into 14 image data stores, corresponding to the 14 classes.

544 Fourteen of the computer keyboard keys were marked with the symbols of the 14 classes in order to expedite the manual

545 classification of the initial training data set. These images were used for initial CNN training. The resulting CNN was used to

546 classify the ICE-CAMERA data set for the years 2014 to 2017. Correctly classified, selected images from this CNN-produced

547 image dataset were manually added to the 14 training image data set as new training images for a second CNN training. Even

548 if many of the images used for the next CNN training and testing had already been classified by the CNN, these images should

549 be considered as ordinary, supervised training images. This process has been repeated recursively three times in order to

550 expand the training database and thus increase the accuracy of the CNN classifier.

551 Figure 16 shows the final number of training and test images selected for each class. The total number of images used for the

552 training was 81800. Trigonal plates were rare, and their number in the training dataset was thus artificially augmented by

553 duplicating the training images, in order to avoid their absence in the small (64-images) training mini-batches.

554
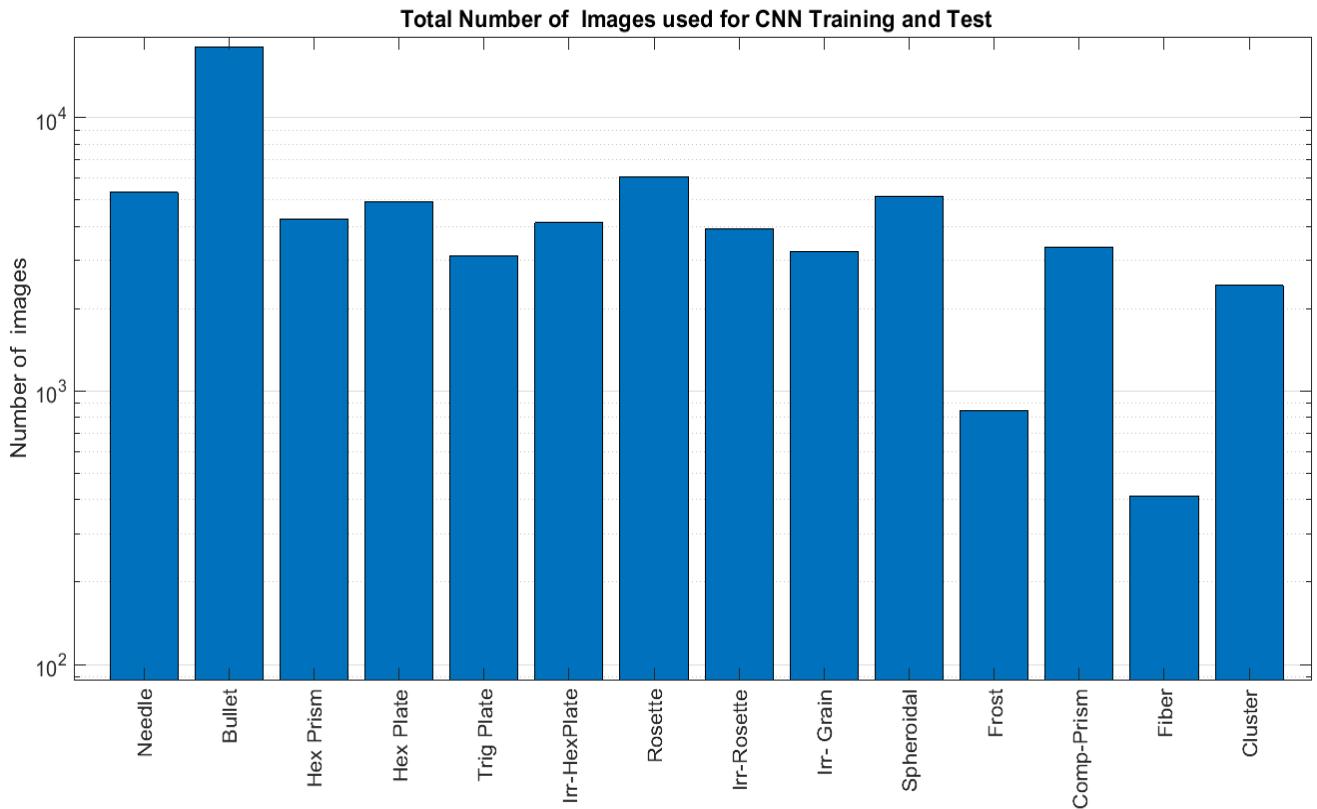
555
556   **Fig. 16: The final number of images used for CNN training + validation + test.**
557
558
559

560 **4.2.3 CNN training details.**

561 To meet Google's input requirements, all images of single particles were resized to 224*224 pixels. In the training process,

562 'data augmentation' was applied to the original data set. Artificially 'augmenting' the image data set has been shown to be

563 effective in CNN training (Shorten and Khoshgoftaar, 2019). Images inside each mini-batch are automatically, randomly

564 'augmented' in order to reduce CNN overfitting. The following transformations were used in augmentation:

565   • X, Y reflection

566   • random X, Y translations ±30 pixels

567   • Random scaling 80-120%

568   Other changes such as rotation have not been introduced since the ICE-CAMERA images to be classified are

569   typically oriented horizontally by the image processing procedure (e.g. Fig. 14)

570 The following learning options were utilized in GoogleNet training:

571

572   Solver: stochastic gradient descent with momentum (SGDM)

573   activation: softmax

574   Number of Epochs=5

575   Learn Rate=0.001

576   Batch Size=64

577   L2 weight regularization factor=0.005

578   Validation frequency= every 30 iterations

579   Shuffle of the data set at every epoch

580   10% of the image data set of Fig. 16 was dedicated to validating, 10% for testing, and the remaining 80% of the training. The

581   evolution of the CNN training in terms of accuracy and losses is presented in Fig. 17. The validation line closely tracks the

582   training line, showing the absence of overfitting.
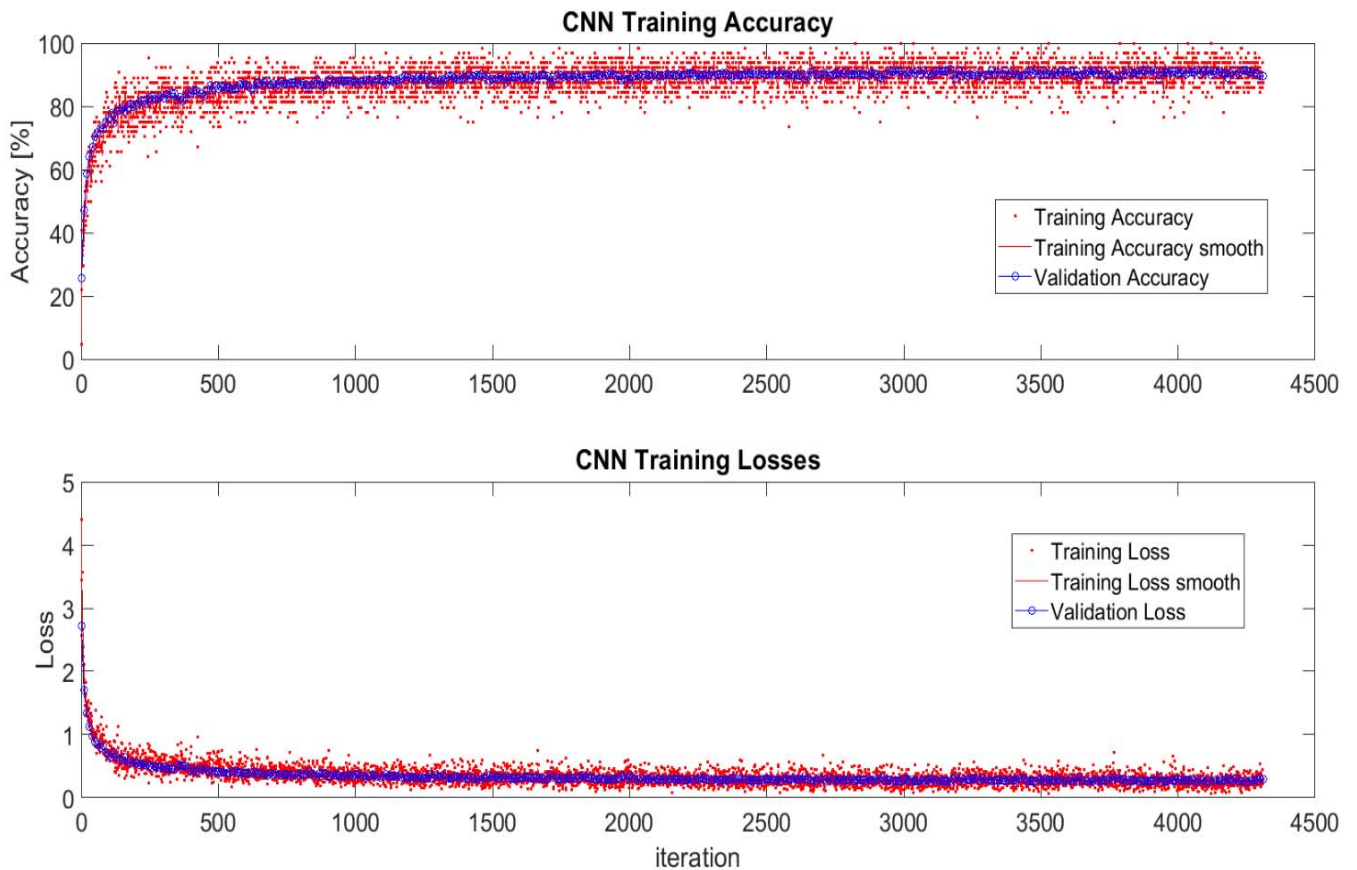
583

584   **Fig. 17: Evolution of the CNN training.**

585

586   **4.2.4. Testing the CNN classifier.**

587   CNN's performance test results are summarized in confusing matrix graphs like Fig. 18a. Each row corresponds to a

588   predicted class (Output Class) and each column corresponds to a true class (Target Class). Diagonal cells refer to correctly

589   classified observations. Off-diagonal cells are improperly classified observations (red color markings increasing

590   misclassification). The column on the far right of the plot shows the percentages of all the examples predicted to belong to

591   each class that are correctly and incorrectly classified (positive predictive value and false discovery rates, respectively). The

592   row at the bottom of the plot shows the percentages of all the examples belonging to each class that are correctly and

593   incorrectly classified (true positive rate and false negative rate, respectively).

594

595

596 **4.2.5 Accuracy of the classifier**.

597 In the column-normalized summary (Fig. 18a), the percentages along the i-th column shows the probability (P) of a "true"

598 particle in class i-th being classified in each of the 14 output classes.
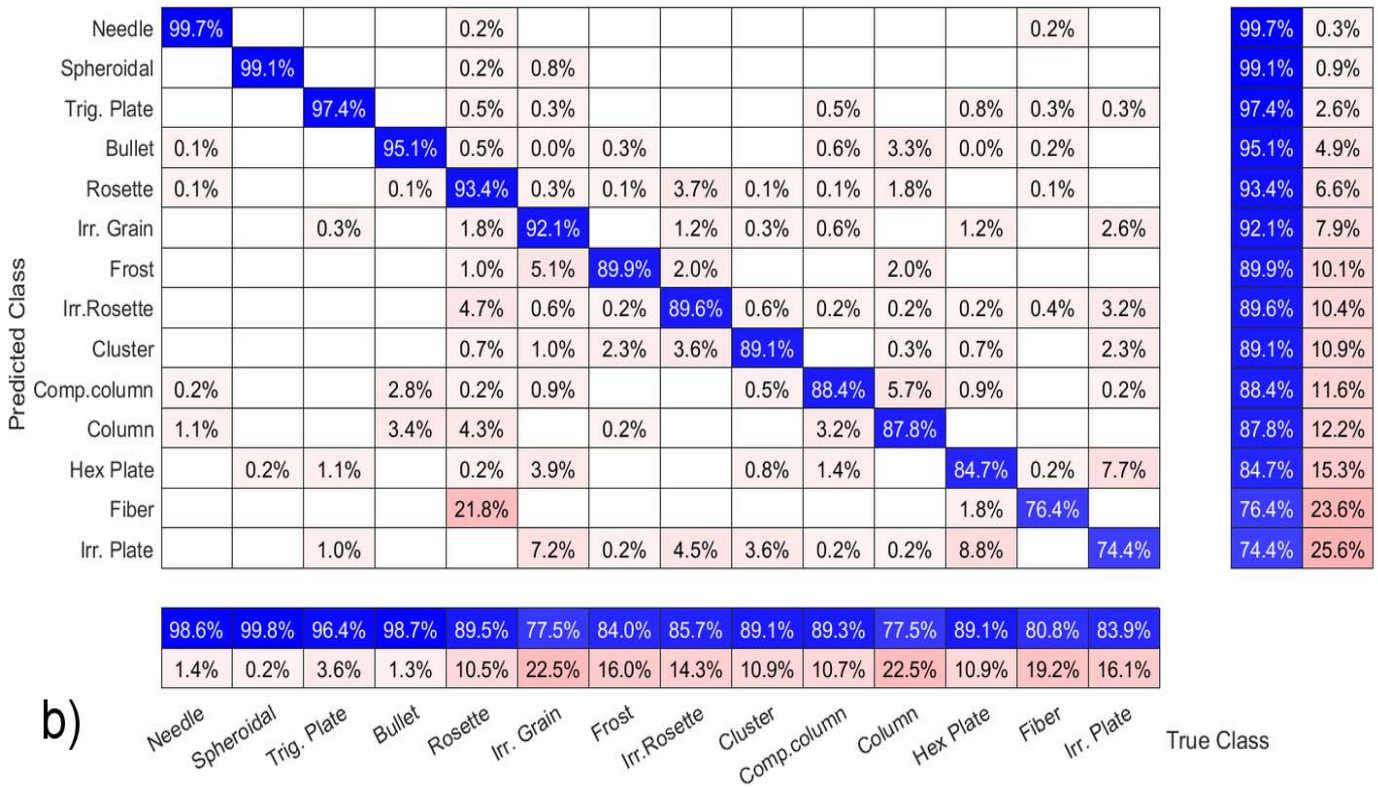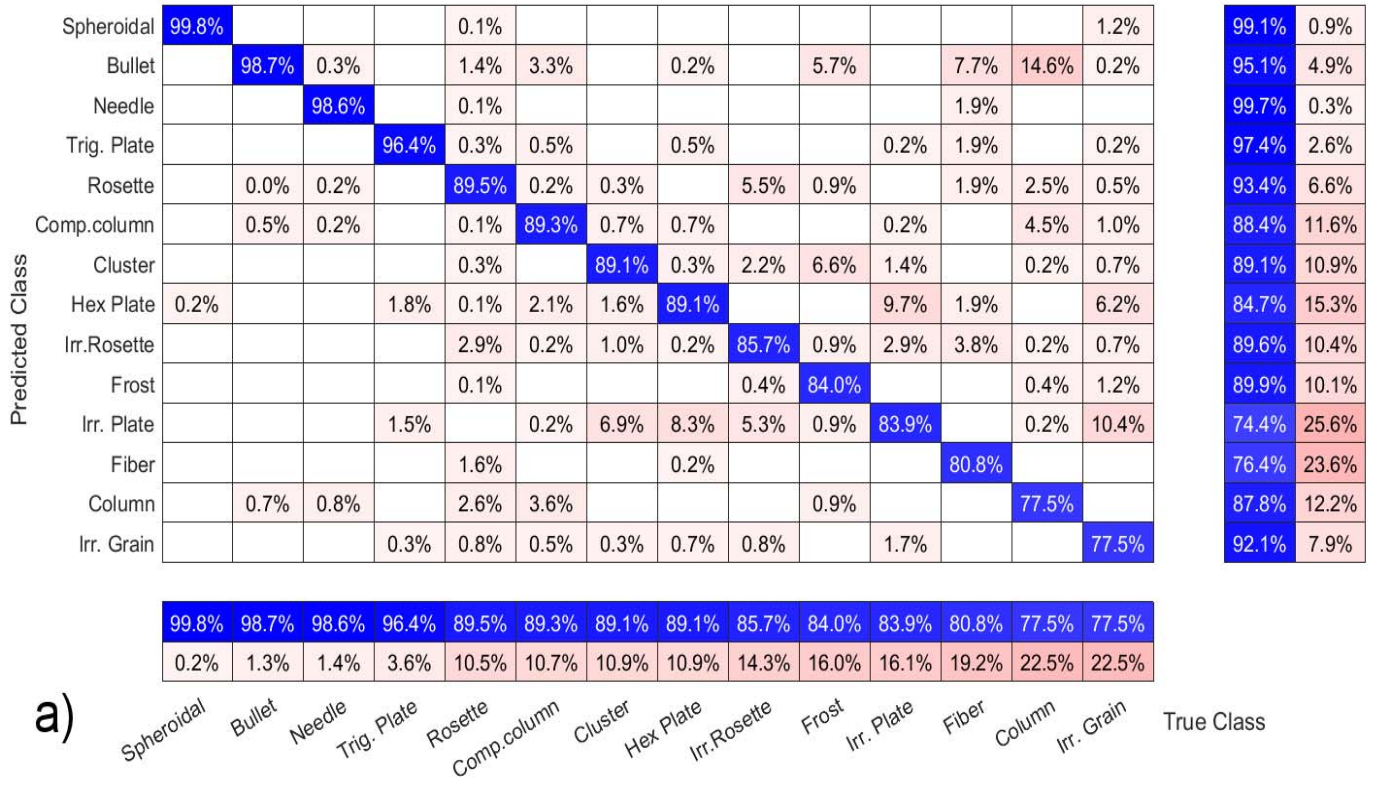
599

600 **Fig. 18: Confusion plot of the CNN :** a) **column-normalized,** b) **row-normalized**

601 Reading the columns of Fig 18a from left to right, the accuracy of the CNN in properly classifying a particle belonging to the

602 i-th true class (bottom row) can be assessed. The results are summarized below:

603

604 -Good accuracy (P>90%) in identifying needles, spheroidal, bullets, trigonal plates.

605 -Compact columns are misclassified into columns (3% of the time) and bullets (3% of the time).

606 -Hexagonal and irregular plates are confused approximately 10% of the time. This is expected since the edges of the plates

607 (usually small) are sometimes blurred in the image.

608 -Irregular rosettes are misclassified in 5% of cases as pristine rosettes and in 5% of cases as irregular plates.

609 -Irregular plates are confused with hexagonal plates 10% of times.

610 -Irregular grains are sometimes mistaken with irregular plates (10%) and hex plates (6%).

611 -Columns are misclassified as bullets 15% of the times.

612 The three-dimensional structure of the ice particles is lost in the ICE-CAMERA images, so that some thick ice forms such as

613 C4a, P1b, G3b, CP1a, etc. (Kikuchi et al, 2013), if any, are likely to be misclassified by this CNN.

614 A different view to read the CNN test is the row-normalized summary of the confusion matrix (Fig. 18b).

615 Percentages along the i-th row now show the probability for a particle classified into the i-th class to effectively belong to

616 each of the 14 true classes. Reading the rows of Fig. 18b from top to bottom, results are:

617 -Particles classified as needles, spheroidal, trigonal plates, bullets, pristine rosettes and irregular grains effectively (P>90%)

618 belong to their class.

619 -Particles classified as irregular rosettes have a 5% chance of being regular rosettes

620 -Particles classified as compact columns have a 6% chance of being columns.

621 -Particles classified as columns have a 4% chance of being a 2-branch rosette and 3% of being bullets or compact columns.

622 -Particles classified as pristine plates have a 4% chance of being irregular grains.

623 -Particles classified as irregular plates have a 7% chance of being irregular grains, 9% hex. plates, and 5% of being irregular

624 rosettes

625 **5. Results.**

626 **5.1 Overview of ICE-CAMERA data set.**

627 From January 2014 to December 2021, ICE-CAMERA has segmented a total of 11.007.543 particles. This gross count includes

628 particulates successively rejected for the statistical analysis. Some whole scans were eventually ignored because of poor focus,

629 sledge motor failures, or the presence of layers of snow or frost. Individual particles were omitted from the analysis due to

630 their small size or defocus. The distribution of the number of particles observed during the months is shown on Fig. 19a. The

631 number of scans per month is shown in Fig.19b. Under optimal conditions, one scan per hour is planned, with a typical total

632 of 740 scans per month. Some months, problems with ICE-CAMERA, focusing, or processing software resulted in the small

633 number of scans or particles observed. In most other cases, scans were not recorded when fewer than ten particles were detected

634 on the DS.

635

636
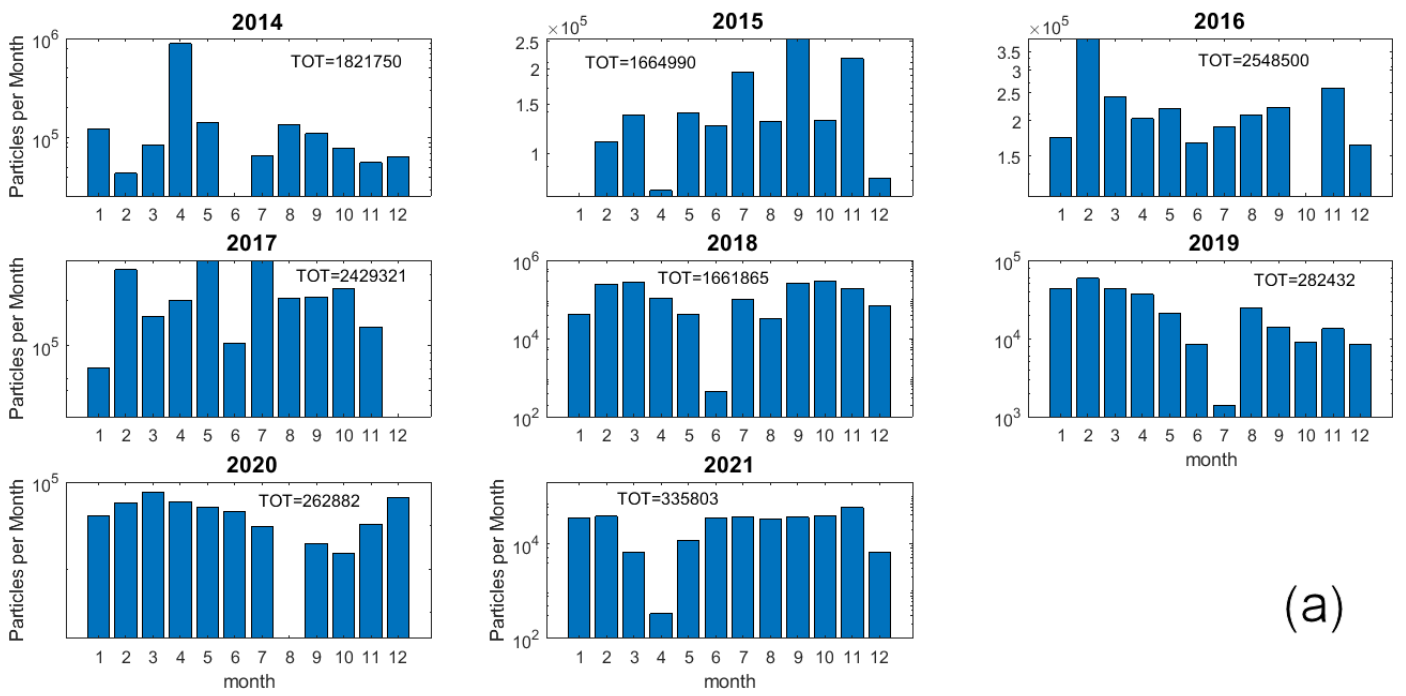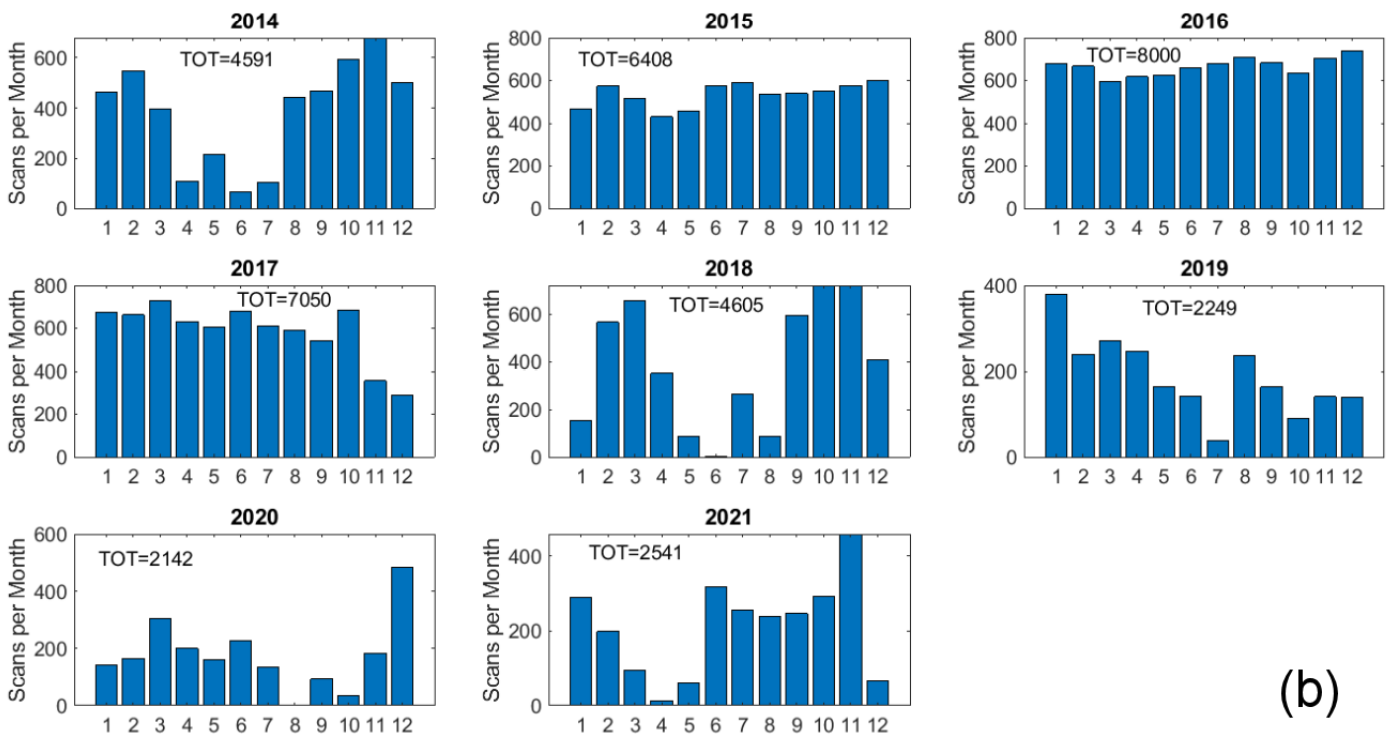
Fig. 19: Statistics per month for the years 2014 to 2021. a) Ice particle counts per month (total counts per year are also reported). (b) Number of scans per month (total number per year is also reported)

639

The number of particles per scan (NpS) is a rough indicator of the intensity of the collected precipitation, but it could be affected by sublimation, because in condition of 'warm' air the smallest particles could disappear from the DS before being detected (sec.3.2). Figure 20a shows the NpS in relation to the air temperature for the whole period 2014-2021, in box and whisker format. On each box, the middle mark indicates the median, and the lower and upper edges indicate the 25th and 75th percentiles, respectively. The lower and upper whiskers indicate an interquartile below the 25th percentile and an interquartile above the 75th percentile.

646 Most ice particles were detected at temperatures between -60°C and -45°C, characteristic temperatures in spring and autumn.

647 The NpS at -70ºC is not statistically different from the NpS at -30ºC. This result suggests that sublimation on the DS during

648 the deposition period is less important than the natural variability of precipitation intensity in determining the number of

649 particles detected during the acquisition. This is confirmed by the DC air temperature statistics (fig.20d): most particles were

650 detected at temperatures above the median DC temperature, whereas. in the case of significant sublimation, we would expect

651 more particles in the lower temperature range (Sect.3.2).

652 A similar consideration can be made when looking at NpS statistics with relative humidity (Fig. 20b). Most particles were

653 detected with relative humidity ranging from 35% to 60%. NpS for RH=20% does not differ statistically from NpS at 80%

654 RH. Even if RH is less important than temperature in determining the sublimation rate, also this result suggests that sublimation

655 does not affect dramatically the *number* of particles finally detected by ICE-CAMERA.

656 Figure 20c shows NpS in relation to wind velocity: ice particles were collected by ICE-CAMERA under all wind conditions

657 encountered in DC. Ice particles were numerically more abundant when the wind was between 7 ms^{-1} and 15 ms^{-1}. As the

658 average surface wind speed at DC resulted around ≈6 m s^{-1} for the measurement period (Fig.20f), particles were collected on

659 the DS preferentially with winds stronger than the average, a condition typically encountered in winter in coincidence with

660 warming events (Argentini et al.,2014). These winds exceed the threshold value of 5 m s^{-1} for blowing snow at ICE-CAMERA

661 altitude, and may ultimately contain some drifting snow. The drop of NpS for wind speeds above 15 m s^{-1} (very rare in DC)

662 is probably due to the limited attachment of snow to the DS with strong winds.

663
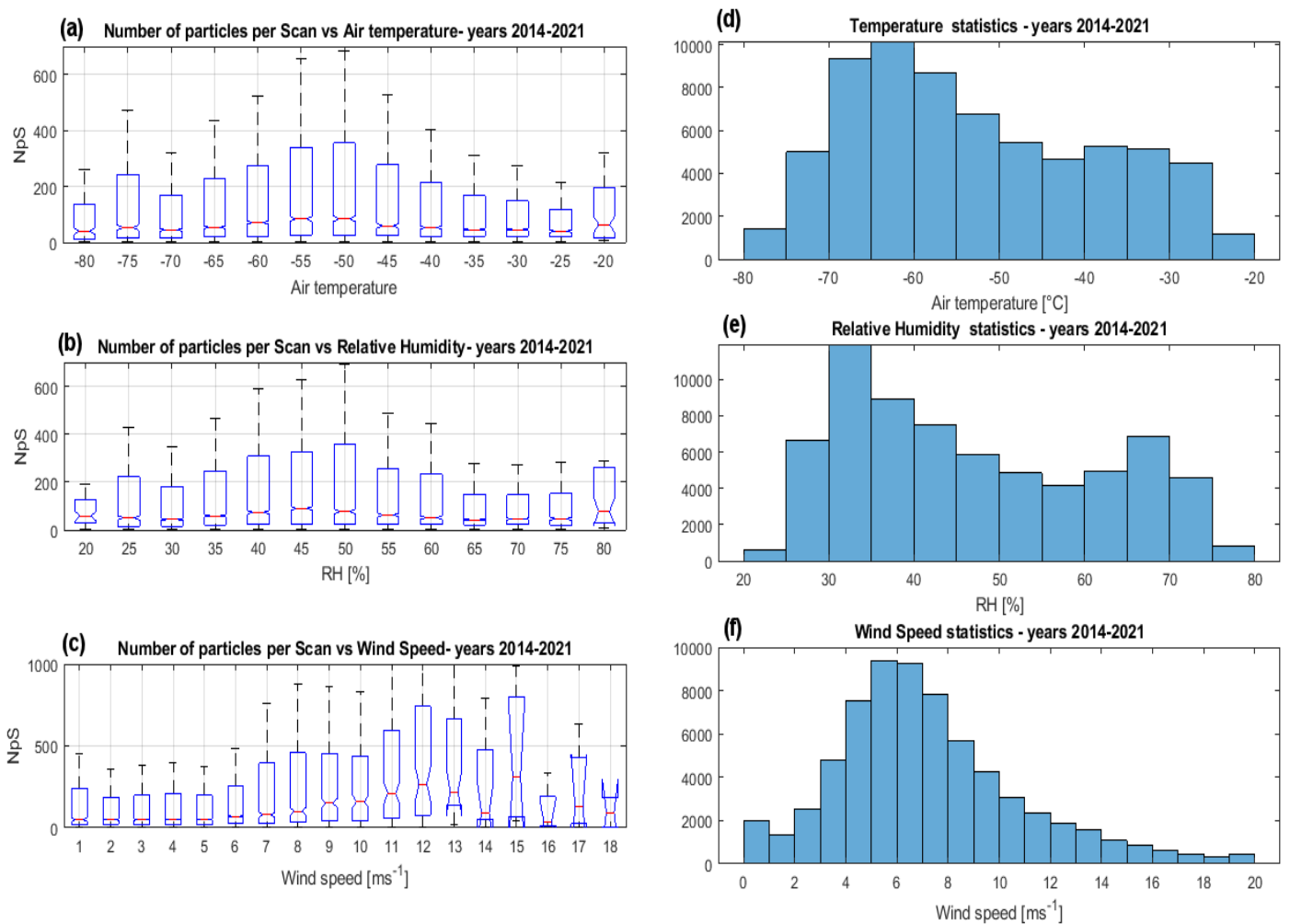
664

665 **Fig. 20: NpS statistics in relation to a)Tair, b) RH , c) wind speed.**

666 **For comparison, the statistics for d)Tair, e) RHy, and f) wind speed are shown for the same period (2014-2021).**

667

5.2 Image processing and CNN used on ICE-CAMERA data.

669 MATLAB post-processing software, including the CNN classifier (Sect.4.2) and measurement tools (Sect.4.1) has been
670 applied to the 2014-2017 ICE-CAMERA dataset. Even if the detailed analysis of these data is the task of a separate paper, a
671 sample of the capacity of the instrument is presented in this section for the first two years of measurement (2014-2015). The
672 total particles analyzed resulted in N=553.358. The number of particles classified in the 14 classes is reported in Fig. 21. The
673 relative rarity of trigonal plates and spheroid particles is evident.
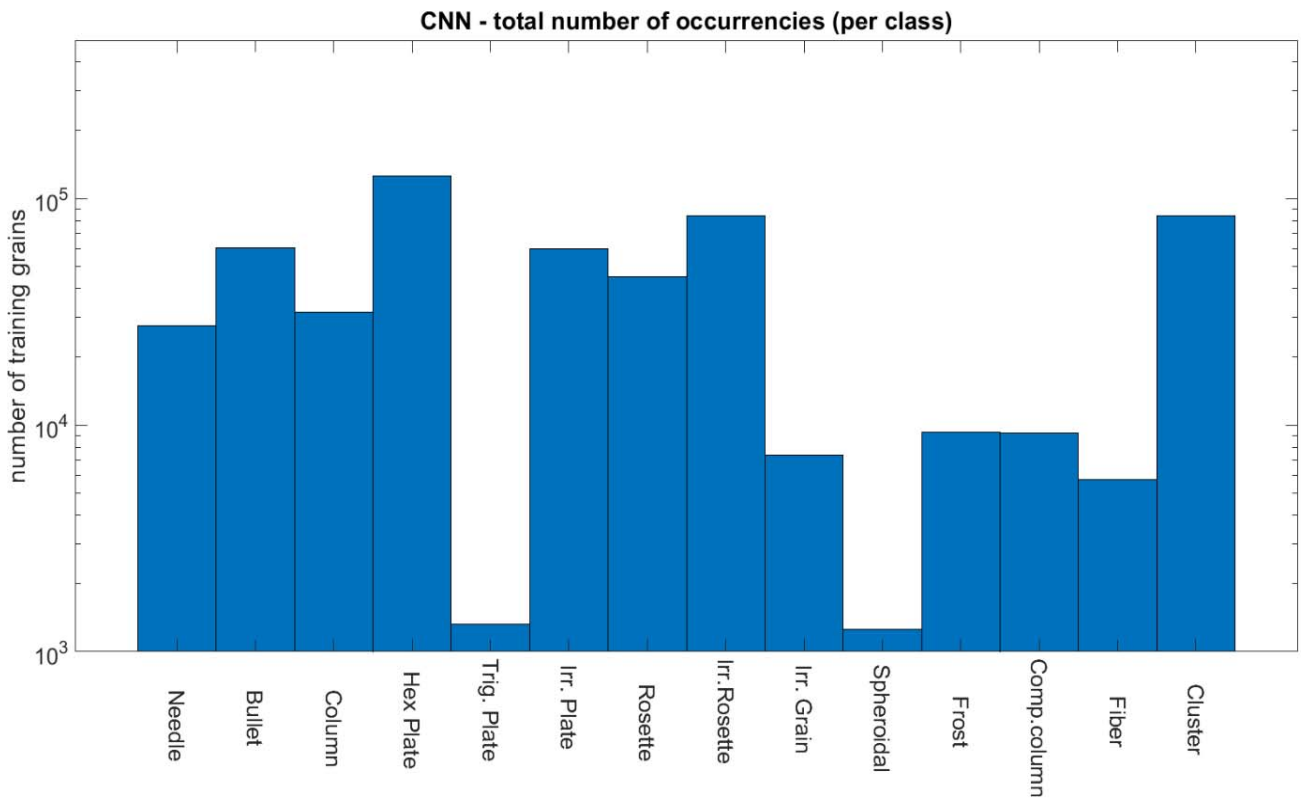
674

675 **Fig. 21: Total numbers of particles classified in the 14 classes for years 2014-2015 .**

676

677 Figure 22 shows the Feret length statistics in box and whisker format. Particles classified as plates, needles, compact columns,
678 spheroidal and irregular grains gave an average length lower than 300 μm. Bullets and columns mean length resulted in the
679 400-500 μm range, while for rosettes and irregular rosettes was in the 350-550 μm range.

680

681

682

683
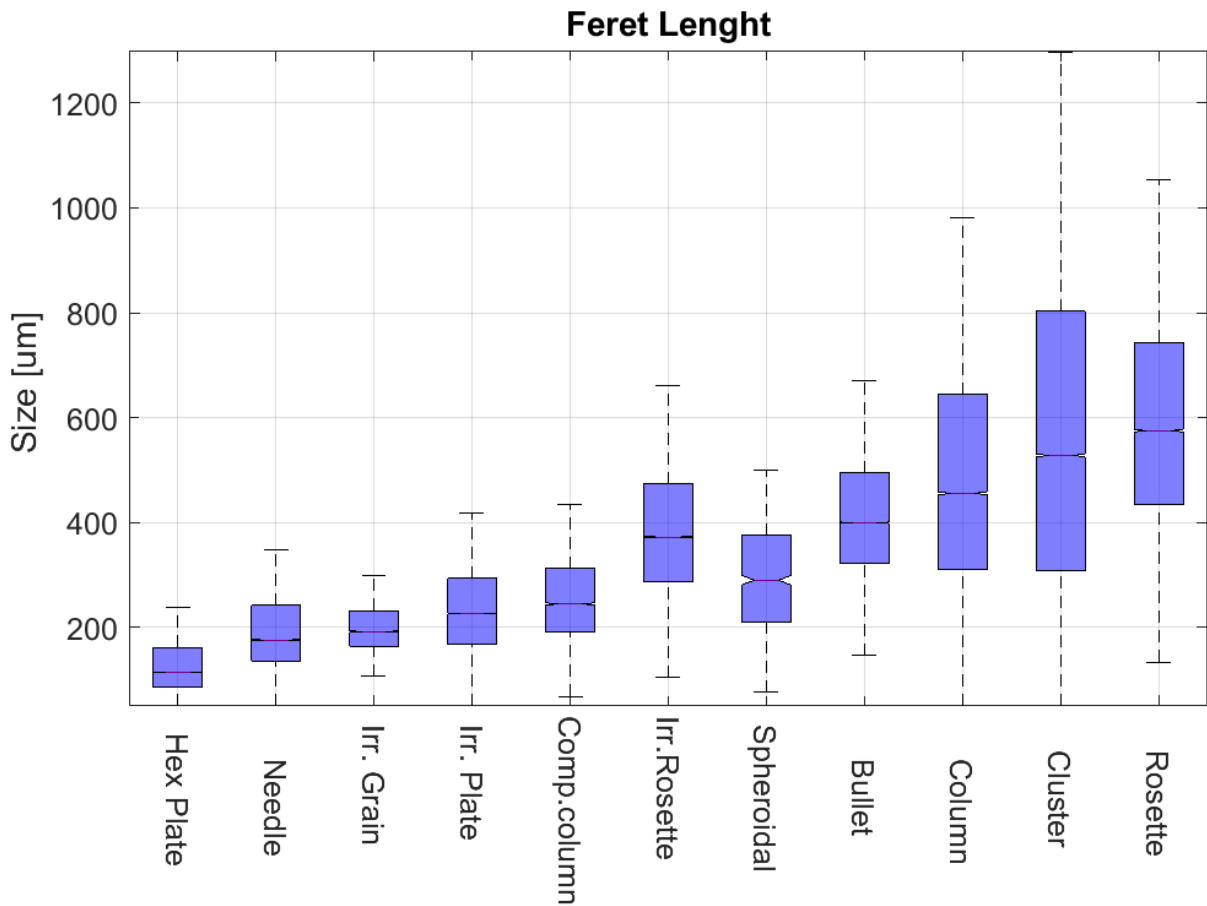
686   **Fig. 22: Feret length statistics for the years 2014-2015**

687   Figure 23 shows in detail the probability distribution of the Feret length for plates and rosettes. For plates (Fig23b), the peak

688   of the distribution is for Lferet=100 μm, similar to the peak of the diamond dust (maximum) size distribution measured by

689   Lawson et al. (2006) at SPS in summer (it must be pointed out that Lawson et al. (2006) measured also particles as small as

690   30 μm , while particles below 60 μm are not processed by the ICE-CAMERA software, and are therefore missing from the

691   probability distribution of Fig23b). This finding indicates that the possible sublimation of particles less than 100-200 μm during

692   the deposition time, suggested in Section 3.2, is not relevant for the final particle size statistics. The results obtained from ICE-

693   CAMERA for pristine rosettes (Fig23a), differ considerably from those of Lawson et al (2006), because the peak of the

694   probability distribution resulted L=480 μm, to be compared with L=120 μm of Lawson et al (2006). This difference is not

695   explicable with the eventual sublimation of the smallest rosettes on the DS. Instead, this result is a realistic feature, sustained

696   by the direct visual observation of rosettes in DC precipitation.

697
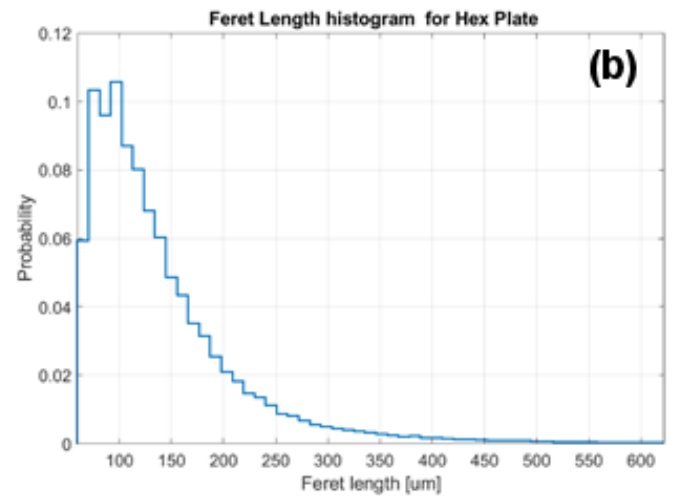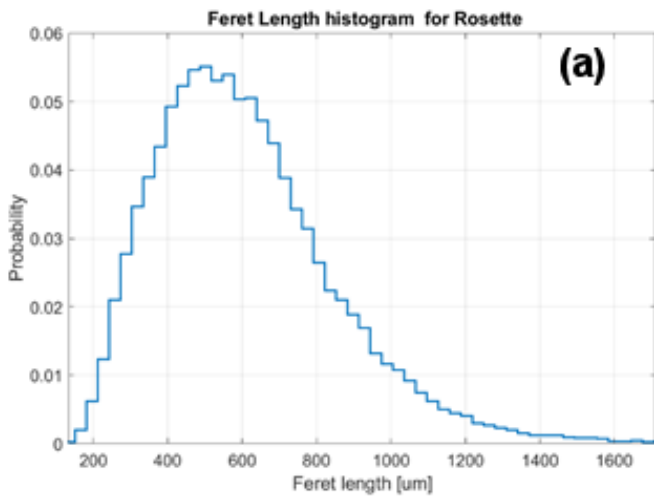
Fig. 23: Feret length probability distribution for a) rosettes and b) hex. plates. The relevant presence of small plates (D<200μm) suggests that sublimation on the DS is not relevant. years 2014-2015

700 Figure 24 shows the trend of the mean Feret length of hexagonal plates with air temperature (sample size=121166 plates).

701 The maximum plate size is observed at temperatures of -30 to -40°C. If sublimation on the DS dominated the size

702 distribution of the plates observed by ICE-CAMERA, an inverse relationship between size and temperature would be

703 expected. This finding again suggests that sublimation on the DS (even in summer, and up to -40°C air temperature) is not as

704 important as numerical simulations might suggest.

705
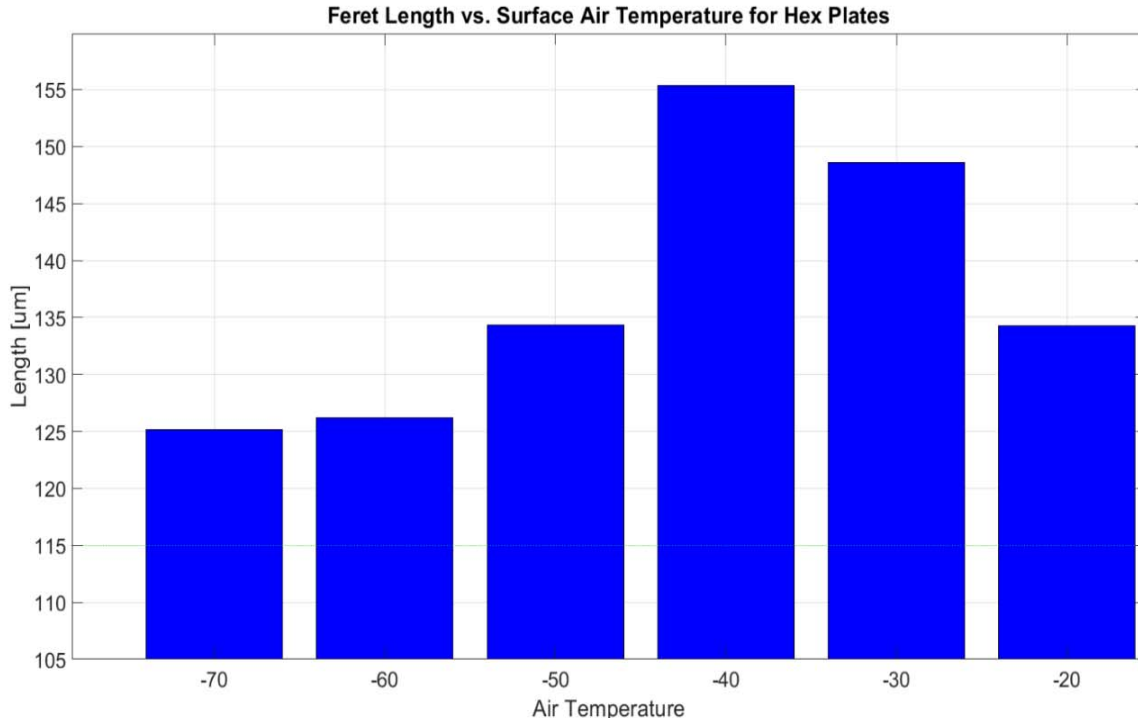
706 **Fig. 24: Average Feret length for hex. plates with respect to air temperature – years 2014 to 2015.**

707 Figure 25a shows Feret's aspect ratio per class. Not surprisingly, many "rounded" classes (plates, rosettes, etc.) have an AR<2.

708 Compact columns show a median AR close to 2.4, while columns and bullets are close to 3. The average AR for the needles

709 was 3.2, which is lower than expected for the reasons outlined in section 4.1.4.
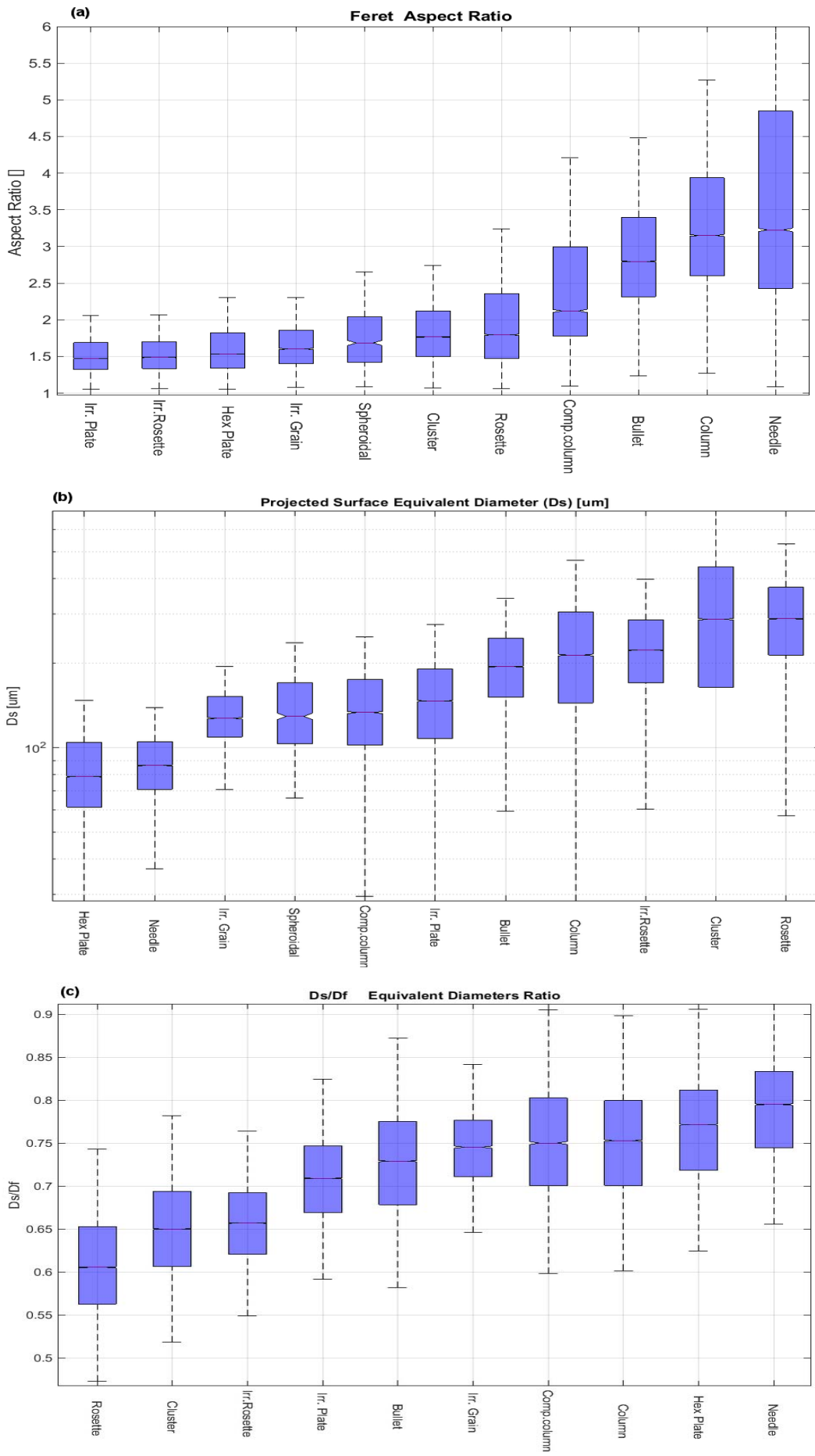
710

711   **Fig. 25: Statistics of : (a) Aspect Ratio, (b) Projected surface-equivalent diameter (Ds), (c) ratio between surface-**

712   **equivalent (Ds) and Feret box-equivalent (Df) diameters for the years 2014-2015.**

713

Figure 25b shows the surface-equivalent diameter Ds of the particles. Figure 25c shows the ratio between the surface

equivalent diameter (Ds) and the bounding box equivalent diameter (Df). The difference between the two diameters is relevant

for "fluffy" particles like rosettes and clusters. For those particles, Ds/Df gave values of 0.6 to 0.65. For comparison, a round

particle is expected to have a ratio of Ds/Df=0.78.

6. Conclusions.

ICE-CAMERA, although very similar to a simple flatbed scanner in its basic design, has represented a technical challenge for

its implementation at DC. Hardware and software have been continuously and extensively modified at DC over the past five

summer campaigns. The result is now a reliable instrument, running throughout the year on an hourly basis, for the statistical

study of precipitation in internal polar areas. Particle size and morphology are automatically obtained, and some semi-

quantitative precipitation estimates can be derived. The collected data are automatically pre-analyzed, but they can be post-

processed at any time, in order to follow the continuous improvements of the image processing and machine learning

algorithms. The GoogleNet CNN, trained specifically for this instrument, has succeeded in classifying ICE-CAMERA images

into 14 form classes, with an accuracy of more than 80% for most of them.   The instrument is particularly useful for

automatically measuring the size of individual ice particles in precipitation, a process virtually impossible manually, and

certainly impossible on the field in DC and elsewhere on the Antarctic plateau in winter. ICE-CAMERA scans are carried out

every hour. Keeping the surface of the instrument free of frost all the time and cleaning it by heating the deposition surface

after each scan is paid with the possible loss of small ice particles. Particles less than 100-200 um can disappear by sublimation

before being recorded, especially in summer. This problem is complementary to the problem encountered when observing

precipitation manually: when observing precipitation manually every 24 hours, (as is the case of DC) the reprocessing of

particles, or the formation of ice and hoar artifacts cannot be prevented. In ICE-CAMERA, frost and ice regrowth are

suppressed, but small particles may disappear for sublimation. ICE-CAMERA data, collected since 2014, have already been

statistically processed and the results will be described in a specialized paper. Results from a subset of data (years from 2014

to 2015), was presented in this work. These results demonstrated the capability of the instrument to classify and size individual

ice particles in DC precipitation, apparently without dramatic losses of small particles for sublimation . Cloud precipitation

particles (rosettes) were found to be significantly larger (480 μm) than those observed at SPS by Lawson et al (2006), while

plates resulted of similar size (120 μm). Unfortunately, only non-polluted, very cold, low humidity, low precipitation

environments (like high mountain tops, dry polar environments) could house a similar instrument. In the presence of pollution,

marine aerosols or dust, manual cleaning of the DS would be required to remove solid particles and salts escaping sublimation.

For coastal zones, the temperature is generally close to zero, making the thermal cleaning of the DS by sublimation

problematic. In these environments, if an instrument like ICE-CAMERA were installed, a mechanical wiper would replace the

heated window of the current instrument. Furthermore, the CNN presented in this paper should be re-trained with different

classes of ice crystals.

7. Technical issues.

Using ICE-CAMERA at DC, as well as other automated instruments, was difficult. The instrument had several failures along

years, and each one was difficult to fix, at least in winter, when the instrument had to be dismounted from the roof of the

shelter at -70°C and eventually fixed in the local lab by the winter-over crew, with remote assistance from Europe. Until a few

years ago, communicating with DC was limited to email with small attachments, making remote assistance a lengthy task.

Even today, connecting the rest of the world remotely with the ICE-CAMERA PC, to operate with the instrument software, is

virtually impossible. Most hardware failures in DC were due to software bugs or computer failures. Rather than having trouble with low temperatures, operating in DC means dealing with limited heat-dissipation of PC parts such as power supply and hard disks, electrostatic discharge issues in low-humidity, heated environments, lack of spare parts for most of the year, a varied skill-ness of winter-over personnel. Failures in the thermal control of ICE-CAMERA caused some mechanical stress and failures in the focusing sledge, while water condensation eventually rusted the bearings of the stepper motors (all bearing were de-greased for a better low temperature operation). The CNN used to classify ICE-CAMERA images is continually changing and improving and the CNN training data set increases with time, as new images collected by ICE-CAMERA are used as new training ones.

8. Code and Data availability.

The CNN developed as part of this work (under Mathworks MATLAB R2020B), along with the image data set (224*224 images for the 14 classes of particles) used for training, validation and testing the CNN are available in the ZENODO repository (Del Guasta, 2022)

Acknowledgements.

I am grateful to the Italian Antarctic Project PNRA for supporting this work with the projects ICE-CAMERA (PNRA 2009/A4.1) and PRE-REC (PNRA 2013/AC3.05). I am also grateful to the 'Osservatorio Meteo-Climatologico Antartico' (PNRA 14_00100) for the Meteo data, and to all the logistics staff and winter-over crews of Concordia station, all working hard to permit our scientific activity. I am also grateful to Francesco Castagnoli (INO CNR) for the initial design of the instrument.

796

797 **References.**

798 Aristidi, E.: An analysis of temperatures and wind speeds above Dome C, Antarctica, Astronomy and Astrophysics, 430, 739–
799 746, https://doi.org/10.1051/0004-6361:20041876, 2005.

800

801 Argentini, S., Pietroni, I., Mastrantonio, G., P., V. A., Dargaud, G., and Petenko, I.: Observations of near surface wind speed,
802 temperature and radiative budget at Dome C, Antarctic Plateau during 2005, Antarct. Sci., 26(1), 104–112,
803 https://doi.org/10.1017/S0954102013000382, 2014.

804

805 Bailey, M.P. , Hallett, J.: A Comprehensive Habit Diagram for Atmospheric Ice Crystals: Confirmation from the
806 Laboratory, AIRS II, and Other Field Studies, J..Atm..Sci., 61, 2888–2899, https://doi.org/10.1175/2009JAS2883.1, 2009.

807 Bracci, A., Baldini, L., Roberto, N., Adirosi, E., Montopoli, M., Scarchilli, C., Grigioni, P., Ciardini, V., Levizzani, V.,Porcù,
808 F.:Quantitative Precipitation Estimation over Antarctica Using Different *Ze-SR* Relationships Based on Snowfall
809 Classification Combining Ground Observations. Remote Sens. 2022, 14, 82. https://doi.org/10.3390/rs14010082, 2022.

810

811 Bromwich, D. H.: Snowfall in high southern latitudes, Rev. Geophys., 26(1), 149–168,
812 https://doi.org/10.1029/RG026i001p00149, 1988.

813 Del Guasta, M.: CNN for the classification of ICE-CAMERA images of Antarctic ice particles, Zenodo [code],
814 https://doi.org/10.5281/zenodo.6822140, 2022.

815

816 Deng,J. Dong,W., Socher R., Li,L-J., Li,K., and Li, F-F.: ImageNet: A large-scale hierarchical image database, IEEE
817 Conference on Computer Vision and Pattern Recognition, 248-255, https://doi.org/10.1109/CVPR.2009.5206848, 2009.

818

819 Eidevåg,T., Abrahamsson, P.., Eng M., and Rasmuson A.,Modeling of dry snow adhesion during normal impact with surfaces,
820 Powder Technology, 361, 1081-1092, https://doi.org/10.1016/j.powtec.2019.10.085, 2020

821

822 Fujita, K., Abe, O.: Stable isotopes in daily precipitation at Dome Fuji, East Antarctica, Geophys. Res. Lett., 33, L18503,
823 https://doi.org/10.1029/2006GL026936, 2006.

824

825 Garrett, T. J., Fallgatter, C., Shkurko, K., Howlett, D.: Fall speed measurement and high-resolution multi-angle photography
826 of hydrometeors in free fall, Atmos. Meas. Tech., 5, 2625–2633, https://doi.org/10.5194/amt-5-2625-2012, 2012

827

828 Genthon, C., Six, D., Gallée, H., Grigioni, P., Pellegrini, A.: Two years of atmospheric boundary layer observations on a 45-
829 m tower at Dome C on the Antarctic plateau, J. Geophys. Res. Atmos., 118, 3218– 3232, https://doi.org/10.1002/jgrd.50128,
830 2016

831

832 Genthon, C., Veron, D. E., Vignon, E., Madeleine, J.-B., Piard, L.: Water vapor in cold and clean atmosphere: a 3-year data
833 set in the boundary layer of Dome C, East Antarctic Plateau, Earth Syst. Sci. Data, 14, 1571–1580,
834 https://doi.org/10.5194/essd-14-1571-2022, 2022.

835

836 Grazioli, J., Tuia, D., Monhart, S., Schneebeli, M., Raupach, T., and Berne, A.: Hydrometeor classification from two-
837 dimensional video disdrometer data, Atmos. Meas. Tech., 7, 2869–2882, https://doi.org/10.5194/amt-7-2869-2014, 2014.

838

839 Grazioli, J., Genthon, C., Boudevillain, B., Duran-Alarcon, C., Del Guasta, M., Madeleine, J.-B. and Berne, A.: Measurements

840 of precipitation in Dumont d'Urville, Adélie Land, East Antarctica, The Cryosphere, 11, 1797–1811,

841 https://doi.org/10.5194/tc-11-1797-2017, 2017.

842

843 Grazioli, J., Madeleine, J.B., Gallée,H., Forbes, R.M, Genthon,C., Krinner ,G., Berne, A. Katabatic Winds Diminish

844 Precipitation Contribution to the Antarctic Ice Mass Balance. *PNAS*, https://doi.org/10.1073/pnas.1707633114, 2017.

845

846 Grazioli, J., Ghiggi, G., Billault-Roux, AC and Berne A.: MASCDB, a database of images, descriptors and microphysical

847 properties of individual snowflakes in free fall. *Sci Data* **9,** 186. https://doi.org/10.1038/s41597-022-01269-7, 2022.

848

849 Ham,F.S.:Shape-preserving solutions of the time-dependent diffusion equation, Quart..Appl.Math. **17**,137-145

850 https://doi.org/10.1090/qam/108196, 1959.

851

852 Heymsfield, A. J., Protat, A., Bouniol, D., Austin, R. T., Hogan, R. J., Delanoë, J., Okamoto, H., Sato, K., van Zadelhoff, G.,

853 Donovan, D. P., Wang, Z: Testing IWC Retrieval Methods Using Radar and Ancillary Measurements with In Situ Data, Journal

854 of Applied Meteorology and Climatology, 47(1), 135-163. Retrieved Jun 28, 2022, https://doi.org/10.1175/2007JAMC1606.1,

855 2008.

856

857 Hiley, M. J. , Kulie, M.S., Bennartz R.: Uncertainty Analysis for CloudSat Snowfall Retrievals, Journal of Applied

858 Meteorology and Climatology, 50, 2 ,399-418, 2011.

859

860 Hogan, A. W.: Summer Ice Crystal Precipitation at the South Pole. ,J. of Appl. Meteorol.,14, 2, 246-248,

861 https://doi.org/10.1175/1520-0450(1975)014<0246:SICPAT>2.0.CO;2, 1975.

862
863

864 Huffman, G. J., Adler, R. F., Morrissey, M. M., Bolvin, D. T., Curtis, S., Joyce, R., McGavock, B., Susskind, J.: Global

865 Precipitation at One-Degree Daily Resolution from Multisatellite Observations. Journal of Hydrometeorology 2, 1, 36-50,

https://doi.org/10.1175/1525, 2001.

866 Hu, MK.: Visual pattern recognition by moment invariants, Information Theory, IRE Transactions, 8, 179-187,

867 https://doi.org/10.1109/TIT.1962.1057692, 1962.

868 Jambon-Puillet, E., Shahidzadeh, N. and Bonn, D.: Singular sublimation of ice and snow crystals. Nature Commun. 9**,** 4191.

869 https://doi.org/10.1038/s41467-018-06689-x, 2018.

870 Kikuchi, K., Hogan A.W.: Properties of Diamond Dust Type Ice Crystals Observed in Summer Season at Amundsen-Scott

871 South Pole Station, Antarctica, J. of the Meteorol. Soc. of Japan. Ser. II, 57, 2, 180-

872 190, https://doi.org/10.2151/jmsj1965.57.2_180, 1979.

873 Kikuchi, K., Kameda, T., Higuchi, K., Yamashita, A.: A global classification of snow crystals, ice crystals, and solid

874 precipitation based on observations from middle latitudes to polar regions, Atmos. Res.,132,460–472,

875 https://doi.org/10.1016/j.atmos.res.2013.06.006, 2013.

876

877   Konishi H., Muramoto K., Shiina T., Endoh T., Kitano K.: Z-R relation for graupels and aggregates observed at Syowa

878   station, Antarctica. Proc. NIPR Symp. Polar Meteorol. Glaciol.,5 ,97-103,1992.

879

880   Lachlan-Cope, T., Ladkin, R., Turner, J., & Davison, P. :Observations of cloud and precipitation particles on the Avery Plateau,

881   Antarctic Peninsula. Antarctic Science, 13(3), 339-348. https://doi.org/10.1017/S0954102001000475,2001.

882   Lamb, D.,Hobbs, P. V.: Growth Rates and Habits of Ice Crystals Grown from the Vapor Phase, Journal of Atmospheric

883   Sciences, 28(8), 1506-1509, https://doi.org/10.1175/1520-0469(1971)028<1507:GRAHOI>2.0.CO;2, 1971.

884   Lawson, R. P., Baker, B. A., Zmarzly, P., O'Connor, D., Mo, Q., Gayet, J., Shcherbakov, V. Microphysical and Optical

885   Properties of Atmospheric Ice Crystals at South Pole Station, Journal of Applied Meteorology and Climatology, 45(11),

886   1505-1524. https://doi.org/10.1175/JAM2421.1, 2006.

887   LeCun, Y., Bengio, Y., Hinton, G.: Deep learning. Nature ,521, 436–444, https://doi.org/10.1038/nature14539, 2015.

888

889   Libbrecht ,K.G.: The physics of snow crystals. Rep. Prog. Phys., 68, 855–895, https://doi.org/10.1088/0034-4885/68/4/R03,

890   2005.

891

892   Libbrecht, K.G.: Physical Dynamics of Ice Crystal Growth. Annual Review of Materials Research. 47.

893   https://doi.org/10.1146/annurev-matsci-070616-124135, 2017.

894

895   Libois, Q., Picard, G., Arnaud, L., Morin, S., and Brun, E.: Modeling the impact of snow drift on the decameter-scale

896   variability of snow properties on the Antarctic Plateau, J Geophys Res Atmos, 119, 662–681,

897   https://doi.org/10.1002/2014JD022361, 2014.

898

899   Lindqvist, H., Muinonen, K., Nousiainen, T., Um, J., McFarquhar, G. M., Haapanala, P., Makkonen, R. and Hakkarainen,

900   H. : Ice-cloud particle habit classification using principal components, J. Geophys. Res., 117, D16206,

901   https://doi.org/10.1029/2012JD017573, 2012.

902

903   Liu, G.,Deriving snow cloud characteristics from cloudsat observations,J. Geophys. Res. Atmos., 113 , D00A09,

904   https://doi.org/ 10.1029/2007JD009766, 2008.

905

906   Magono, C., Lee, C. W.: Meteorological classification of natural snow crystals. J. of the Faculty of Sci., Hokkaido

907   University. Series 7, Geophysics, 2(4), 321-335, 1966.

908

909   Nelson, J.: Sublimation of Ice Crystals, Journal of the Atmospheric Sciences, 55(5), 910-919. https://doi.org/10.1175/1520-

910   0469(1998)055<0910:SOIC>2.0.CO;2, 1988.

911

912   Ohtake, T. and Yogi T.: Winter ice crystals at the South Pole. Antarct. J. U.S., 14, 201–203, 1979.

913

914   Palerme, C., Kay, J. E., Genthon, C., L'Ecuyer, T., Wood, N. B., and Claud, C.: How much snow falls on the Antarctic ice

915   sheet?, The Cryosphere, 8, 1577–1587, https://doi.org/10.5194/tc-8-1577-2014, 2014.

916

917 Palerme,C., Claud C., Dufour,A., Genthon,C., Wood N.B., L'Ecuyer,T.: Evaluation of Antarctic snowfall in global
918 meteorological reanalyses, Atmospheric Research, 190, 104-112, https://doi.org/10.1016/j.atmosres.2017.02.015,2017.
919

920 Pratt, W. K.: Digital Image Processing: PIKS Scientific Inside, Fourth Edition, John Wiley & Sons, Inc., Los Altos,
921 California, https://doi.org/10.1002/0470097434, 2006.
922

923 Praz, C., Roulet, Y.-A., and Berne, A.: Solid hydrometeor classification and riming degree estimation from pictures collected
924 with a Multi-Angle Snowflake Camera, Atmos. Meas. Tech., 10, 1335–1357, https://doi.org/10.5194/amt-10-1335-2017,
925 2017.
926

927 Ryzhkin I.A.,Petrenko V.F., Physical Mechanisms Responsible for Ice Adhesion, *J. Phys. Chem. B* 1997, 101, 32, 6267–6270,
928 https://doi.org/10.1021/jp9632145,1977.
929

930 Russ, J.C. and Brent Neal, F.: The Image Processing Handbook 7th Edition, CRC Press, pp 1053,
931 https://doi.org/10.1201/b18983, 2017.
932

933 Santachiara, G., Belosi, F., Prodi, F.: Ice crystal precipitation at Dome C site (East Antarctica), Atmos. Res. 167, 108-117,
934 https://doi.org/10.1016/j.atmosres.2015.08.006, 2016.
935

936 Satow, K.: Observations on the Shapes of Snow Crystals in the Summer Season in Mizuho Plateau, Antarctica, Memoirs of
937 National Institute of Polar Research. Special issue, 29, 103-109, 1983.

938 Schlosser, E., Dittmann, A., Stenni, B., Powers, J. G., Manning, K. W., Masson-Delmotte, V., Valt, M., Cagnati, A.,
939 Grigioni, P., Scarchilli, C.: The influence of the synoptic regime on stable water isotopes in precipitation at Dome C, East
940 Antarctica, The Cryosphere, 11, 2345–2361, https://doi.org/10.5194/tc-11-2345-2017, 2017.

941 Schmidhuber, J.: Deep Learning in Neural Networks: An Overview. Neural Networks, 61, 85-
942 117,https://doi.org/10.1016/j.neunet.2014.09.003, 2014.
943

944 Schneider, U., Finger, P., Meyer-Christoffer, A., Rustemeier, E., Ziese, M., Becker, A.: Evaluating the Hydrological Cycle
945 over Land Using the Newly-Corrected Precipitation Climatology from the Global Precipitation Climatology Centre
946 (GPCC). *Atmosphere* **2017**, *8*, 52. https://doi.org/10.3390/atmos8030052, 2017.
947

948 Shorten, C., Khoshgoftaar, T.M.: A survey on Image Data Augmentation for Deep Learning. *J Big Data* 6, 60,
949 https://doi.org/ 10.1186/s40537-019-0197-0, 2019.

950 Shimizu, H., ''Long prism'' crystals observed in the precipitation in Antarctica. J. Meteor. Soc. Japan, **41,** 305–307.
951 https://doi.org/10.2151/jmsj1923.41.5_305, 1963.
952

953 Smiley, V. N., Whitcomb, B. M., Morley, B. M., & Warburton, J. A.: Lidar Determinations of Atmospheric Ice Crystal
954 Layers at South Pole during Clear-Sky Precipitation. Journal of Applied Meteorology, 19,9, 1074–1090, 1980.
955

956 Souverijns,N., Gossart,A., Lhermitte, S., Gorodetskaya I.V., Kneifel,S., Maahn,M., Bliven,F.L., van Lipzig,.P.M.:Estimating

957 radar reflectivity - Snowfall rate relationships and their uncertainties over Antarctica by combining disdrometer and radar

958 observations, Atmospheric Research,196, 211-223, https://doi.org/10.1016/j.atmosres.2017.06.001.2017,2017.

959 Szegedy,C ., Liu,W., Jia,Y., Sermanet P., Reed S.,, Anguelov D., Erhan D., Vanhoucke V. and Rabinovich A.: "Going

960 deeper with convolutions," 2015 IEEE Conference on Computer Vision and Pattern Recognition (CVPR), 1-9,

961 https://doi.org/10.1109/CVPR.2015.7298594, 2015.

962 Tremblin, P., Minier,V., Schneider,N., Durand, G. Al. , Ashley, M. C. B. , Lawrence, J. S. , Luong-Van, D. M. , Storey,

963 J. W. V. , Durand, G. An. , Reinert, Y., Veyssiere, C., Walter, C., Ade, P. , Calisse, P. G., Challita, Z. , Fossat, E. ,

964 Sabbatini, L., Pellegrini, A., Ricaud, P., Urban, J. : Site testing for submillimetre astronomy at Dome C, Antarctica, A&A

965 535 A112, https://doi.org/10.1051/0004-6361/201117345, 2011.

966 Vignon, E., Genthon, C., Barral, H., Amory, C., Picard, G., Gallée, H., Casasanta, G., and Argentini, S.: Momentum and heat

967 flux parametrization at Dome C, Antarctica: a sensitivity study, Boundary-Layer Meteorol, 162, 341–367,

968 https://doi.org/10.1007/s10546-016-0192-3, 2016.

969 Vignon, E., Genthon, C., Barral, H.,Amory, C., Picard, G., Gallée, H., Casasanta, G., Argentini, S.: Momentum- and Heat-

970 Flux Parametrization at Dome C, Antarctica: A Sensitivity Study. Boundary-Layer Meteorology. https://doi.org/

971 10.1007/s10546-016-0192-3, 2017.

972 Walden, V. P., Warren, S. G., Tuttle, E. (2003). Atmospheric Ice Crystals over the Antarctic Plateau in Winter, Journal of

973 Applied Meteorology, 42(10), 1391-1405,https://doi.org/10.1175/1520-0450(2003)042<1391:AICOTA>2.0.CO;2, 2003.

974 Walton,W.: Feret's Statistical Diameter as a Measure of Particle Size, Nature, **162,** 329–330,

975 https://doi.org/10.1038/162329b0, 1948.

976

977 Xiao, H., Zhang, F., He, Q., Liu, P., Yan,F., Miao, L. and Yang, Z. : Classification of ice crystal habits observed from airborne

978 Cloud ParticleImager by deep transfer learning., Earthand Space Science, 1877–1886, https://doi.org/10.1029/2019EA000636,

979 2019.

980

981 Wood, N., L'Ecuyer, T., Heymsfield, A. , Stephens, G. : Microphysical Constraints on Millimeter-Wavelength Scattering

982 Properties of Snow Particles. Journal of Applied Meteorology and Climatology. 54. 909-931. https://doi.org/10.1175/JAMC-

983 D-14-0137.1, 2015.

984

985 Zheleznyak, A.G. , Sidorov, V.G.: Flatbed scanner as an instrument for physical studies,St. Petersburg Polytechnical

986 University Journal: Physics and Mathematics, 1, Issue 2, 134-141,https://doi.org//10.1016/j.spjpm.2015.04.001. 2015.

987